Experimental Investigation of the Power Amplifiers' Nonlinearity using a 3.5 GHz 2×2 RF Front-end Prototype

by

Yujuan Zhang

A thesis
presented to the University of Waterloo
in fulfillment of the
Master of Applied Science
in
Electrical and Computer Engineering

Waterloo, Ontario, Canada, 2020

AUTHOR'S DECLARATION

I hereby declare that I am the sole author of this thesis. This is a true copy of the thesis, including any required final revisions, as accepted by my examiners.

I understand that my thesis may be made electronically available to the public.

Abstract

Next generation communication systems will demand extremely high system capacity. Approaches such as complex digital modulation schemes, widening of the instantaneous bandwidth and massive multi-input multi-output (MIMO) architectures will need to be employed to realize such high capacity systems. However, these approaches impose stringent requirements on the radio hardware. For instance, in conventional wireless transmitters, isolators/circulators are typically used to immunize the radio hardware and its performance from negative effects of the antenna load variation. However, in massive MIMO transmitters, while the antenna active impedance varies significantly, isolators cannot be used due to their unacceptable overhead in terms of cost and space. Thus, within these transmitters the power amplifiers' (PA) performance in the aspects of linearity, output power and efficiency are significantly impacted by the load modulation introduced by the finite isolation between the antenna elements. To date, studies in the literature have mainly relied on emulating the load modulation in massive MIMO transmitters and have used generic PAs rather than those specifically designed for massive MIMO transmission.

This work begins by designing a two-by-two RF front-end for a massive MIMO transmitter, comprised of antenna and PA arrays suitable for use in a base station. The antenna array is formed of multilayered patch antenna elements that achieved an enhanced isolation and extended fractional bandwidth of 19 dB and 14%, respectively. The PA array was built using gallium nitride transistors and carefully operated in Class J mode. Under continuous wave measurements, the PA array element demonstrated high peak-power efficiency of between 54%-66% over the frequency band ranging from 3.2GHz to 3.8GHz. It also showed excellent linearizability when driven with modulated signals with 200 MHz instantaneous bandwidth. When both the antenna and PA arrays are connected, they form a front-end that was used to study the effects of the antenna load modulation using realistic modulated signals. This study undertook a large set of measurement configurations specifically devised to investigate the effects of coupling due to the PA substrate and finite isolation between the antenna elements, as well as the extent of the nonlinearity of the PA elements. Furthermore, a single-input single-output (SISO) digital pre-distortion (DPD) scheme was applied to attempt to linearize the overall response of the PA array. This study revealed that the coupling attributed to the PA substrate had a minor impact on the array's performance. Furthermore, it highlighted the necessity of jointly designing for both the PA element linearity and the antenna isolation level, so that SISO DPD can be used and MIMO DPD is avoided.

Acknowledgements

First of all, I would like to thank my supervisor Professor Slim Boumaiza for providing me with the valuable opportunity to study and work in Emerging Radio Systems Group (EmRG). Prof. Boumaiza has been giving me academic guidance constructively and encouragement throughout my research.

Moreover, I would like to thank my colleagues, Yue Li for his instructive teaching and advice during my course studying and project design stage based on his deep insight in theories, Ayman Jundi for his beneficial mentoring and support on my project implementation, Mohammed Almoneer for his DPD setup during measurements, Jingjing Xia for his help with device assembling and lab support, and Hai Huang for his enlightenment on scientific methodologies on various topics.

Table of Contents

AUTHOR'S DECLARATION ii
Abstract iii
Acknowledgements iiv
List of Figures vii
List of Tables x
List of Abbreviations x
Chapter 1 Introduction 1
1.1 Motivation 1
1.2 Problem statement 2
1.3 Thesis Organization 3
Chapter 2 Background 4
2.1 PA nonlinearity 4
2.2 Digital Pre-distortion 6
2.3 Literature review of study on cross coupling in MIMO transmitter 6
2.4 Thesis objectives 16
Chapter 3 Antenna array design 18
3.1 Single wideband antenna 19
3.1.1 One layer antenna 20
3.1.2 Stacked Microstrip patch antenna 21
3.2 Wideband high isolation antenna array 22
3.3 Antenna measurement 29
3.4 Conclusion 32
Chapter 4 Power amplifier array design 33
4.1 PA fundamentals 33
4.1.1 Power amplifier basic specifications 33
4.1.2 Operation mode of power amplifier 33
4.1.3 Continuous Class-B Operation (Class J operation) 37
4.2 Single way PA design 39
4.2.1 Output matching 39
4.2.2 Input matching and stability 41
4.2.3 EM simulation and layout 42

4.3 PA array design 44
4.3.1 Four-way PA layout 44
4.3.2 Four-way PA-Antenna simulation 44
4.4 PA measurement 48
4.4.1 Continuous Wave (CW) measurement 48
4.4.2 Modulated signal measurement for single PA 54
4.5 Conlcusion 56
Chapter 5 System measurement and analysis 57
5.1 PA board coupling effect investigation 57
5.2 Antenna coupling effect investigation 58
5.3 Investigation for different isolation level and the extent of PA nonlinearity 60
Chapter 6 Conclusion and future work 64
6.1 Conclusion 64
6.2 Future work 65
Reference 66

List of Figures

Fig. 2.1 AM/AM and AM/PM vs. Drain efficiency (DE) of a Class AB Gallium Nitride (GaN) PA ... 4
Fig. 2.2 AM/AM and AM/PM of a GaN PA with 100MHz 8 dB PAPR OFDM signal ... 5
Fig. 2.3 Spectrum regrowth and in-band distortion ... 5
Fig. 2.4 Block diagram of PA model ... 6
Fig. 2.5 Block diagram of PA compensated by DPD ... 6
Fig. 2.6 Active impedance embodied with reflection coefficient of the PA in MIMO transmitter ... 7
Fig. 2.7 MIMO transmitter with CO-DPD and nonlinear crosstalk [7] ... 8
Fig. 2.8 a) Measurement setup with different insertion of couplers b) measured power spectral density versus frequency for DPD of a DUT with -20 dB linear crosstalk. The different invers model used for DPD are ex-plained in the legend.[8] ... 9
Fig. 2.9 Proposed measurement setup for emulation of coupling effect [10] ... 10
Fig. 2.10 (a) Proposed measurement setup to emulating load mismatch and mutual coupling effect (b) Two-port power amplifier (c) Transmitting front end with mutual coupling [11] ... 11
Fig. 2.11 a) Equivalent model for the dc current generation. b) simulated and measured PA behavior when hav-ing different input phases.[13] ... 13
Fig. 2.12 Spectra of PA1 for (a) high-coupling array and (b) low-coupling array. Left: PA is operated in a single-path scenario. Right: MIMO scenario. Measurements (meas) without SISO DPD and with SISO DPD are com-pared with simulations (sim) without SISO DPD and with SISO DPD.[14] ... 14
Fig. 2.13 Block diagram of a multi-antenna transmitter with the proposed DPD method [15] ... 15
Fig. 2.14. Simulated AM/AM distortion in each of the 64 transmitter PAs. Contour plots to the right show max-imum dB deviation from constant gain. [16] ... 16
Fig. 3.1 Antenna array showing different coupling levels ... 18
Fig. 3.2 Top view (a) and side view (b) of two layer antenna ... 20
Fig. 3.3 top and side view of the one layer antenna ... 21
Fig. 3.4 Simulated S-parameter a) and radiation pattern for phi=0 (red) and 90 degree (blue) b) of the stacked antenna ... 21
Fig. 3.5 Top and side view of Stacked Microstrip patch antenna ... 22
Fig. 3.6 Simulated S-parameter a) and radiation pattern for phi=0 (red) and 90 degree (blue) b) of the stacked antenna ... 22
Fig. 3.7 Evolution of the proposed decoupling unit cell. ... 24

Fig. 3.8 S-parameter characteristics of the loop resonator [34] 24
Fig. 3.9 Loop resonator dimensions 24
Fig. 3.10 Top view of two by two antenna array with loop resonators 24
Fig. 3.11 (a) Simulated S-parameters without loop resonators b) Simulated S-parameters with loop resona-tors. c) Simulated radiation pattern without loop resonators for phi=0 degree (red) and 90 degree (blue).d) Simulated radiation pattern with loop resonators for phi=0 degree (red) and 90 degree (blue) 25
Fig. 3.12 (a) Rogers 5880 stack-up for highly isolated array (b) S-parameters of highly isolated antenna array 27
Fig. 3.13 Active S-parameters and passive S-parameters of low isolation array (a, c, e, g) and high isolation ar-ray (b, d, f, h) for different power ratio of input stimulus: 0 dB (a, b), 10 dB (c, d), 20 dB (e, f) and 30 dB (g, h) 28
Fig. 3.14 One element antenna measurement and simulation. 30
Fig. 3.15 Picture of the antenna array and test environment. 30
Fig. 3.16 Measured 4-port S-parameters of antenna array 31
Fig. 3.17 Measurement (solid line) vs. simulation (dot line) for one element of antenna array 31
Fig. 4.1 Transistor ideal model as VCCS 34
Fig. 4.2 DCIV characterization of transistor 34
Fig. 4.3 Class A operation mode 35
Fig. 4.4 Reduction conduction angle operation mode 36
Fig. 4.5 Class J design space illustrated in Smith Chart including fundamental impedance (blue) and second harmonic (red). 38
Fig. 4.6 Compact small signal model of packaged transistor 39
Fig. 4.7 Antenna impedance plot at fundamental, second, and third harmonic frequency, used for PA output matching design 40
Fig. 4.8 Intrinsic Drain impedance plot at fundamental, second, and third harmonic frequency 41
Fig. 4.9 Single way PA layout with lumped elements denoted 42
Fig. 4.10 CW simulation results for 50 Ohm loaded case (a) Drain efficiency (b) AM-AM (c) AM-PM 42
Fig. 4.11 CW simulation results for Antenna loaded case (a) Drain efficiency (b) AM-AM (c) AM-PM 43
Fig. 4.12 A possible integration stack-up for PA and Antenna 43

Fig. 4.13 PA array layout 44
Fig. 4.14 PA CW performance variation when steering for 30 degree at 3.5 GHz 46
Fig. 4.15 PA CW performance variation when having randomly selected phases at 3.5 GHz 48
Fig. 4.16 (a) PA board (b) CW measurement setup 45
Fig. 4.17 Small signal performance for the PA array 50
Fig. 4.18 Measured large signal CW performance for single way PA with 50 Ohm load 51
Fig. 4.19 Measured large signal CW performance for PA array with 50 Ohm load 52
Fig. 4.20 Modulated signal measurement setup for one PA 54
Fig. 4.21 Modulated signal measurement with 50 Ohm load (a) Continuous 100MHz (b) Continuous 200MHz (c) 150 MHz carrier aggregated signal by 50MHz “101” (d) 200 MHz carrier aggregated signal by 50MHz “1001” 55
Fig. 5.1 PA array modulated signal measurement setup with 50 Ohm loaded 58
Fig. 5.2 PA array modulated signal measurement setup with antenna load 59
Fig. 5.3 PA array modulated signal measurement setup with antenna load and the insertion of attenuators 61
Fig. 5.4 Simulation of the attenuator insertion in antenna array. (a) -19 dB isolation. (b)-28 dB isolation. (c) -19 dB isolation with 9 dB attenuation. 62

List of Tables

Table 4.1 Single PA modulated signal measurement with 50 Ohm load 55
Table 5.1 PA array modulated signal measurement with 50 Ohm load 58
Table 5.2 PA array modulated signal measurement with antenna load 60
Table 5.3 ACPR in dB after SISO DPD with 20MHz OFDM signal for different isolation levels and initial PA nonlinearity 63
Table 5.4 ACPR in dB after SISO DPD with 100MHz OFDM signal for different isolation levels and initial PA nonlinearity 63

List of Abbreviations

MIMO	Multi-input multi-output
PA	Power amplifier
SISO	Single-input single-output
DPD	Digital pre-distortion
5G	Fifth generation
IoT	Internet of things
QAM	Quadrature amplitude modulation
OFDM	Orthogonal frequency division multiplexing
ACPR	Adjacent channel power ratio
GaN	Gallium nitride
CW	Continuous wave
DE	Drain efficiency
NMSE	Normalized mean square error
GMPNLC	Generalized memory polynomial for nonlinear crosstalk
GMPLC	Generalized memory polynomial for linear crosstalk
DUT	Device under test
WCDMA	Wideband code division multiple access
PHD	Poly-harmonic distortion
VSWR	Voltage standing wave ratio
CTMM	Crosstalk and mismatch model
EIRP	Equivalent isotropically radiated power
EM	Electromagnetic
LDMOS	Laterally diffused metal-oxide semiconductor
HEMTs	High-electron-mobility-transistors
VCCS	Voltage-control-current-source

Chapter 1
Introduction

1.1 Motivation

The fifth generation (5G) communication system is expected to be the dominant communication technology, supporting diverse applications including but not limited to Internet of Things (IoT), high-definition videos and enhanced broadband mobile services [1]. Accordingly, unprecedented challenges need to be addressed. For example, large capacity transmission (100 Mbps ~1 Gbps), end-to-end low latency (1 ms) and energy-efficient ultra-dense cover (1 million connections per square kilometer) are the key performance indicators [2].

The demand for high throughput and high signal quality leads to making efficient use of precious and crowded radio spectrum imperatively. On the one hand, employing spectrum efficient modulation scheme such as high-order quadrature amplitude modulation (QAM) in combination with orthogonal frequency division multiplexing (OFDM) exploit the spectrum potential. On the other hand, massive Multiple-Input Multiple-Output (MIMO) technique, integrating large number of active antenna and multiple signal chains at both transmitter and receiver ends, is a very promising solution to achieve the system capacity requirement in many ways. Firstly, the combination of multiple beams in the far field provides the high directivity and high robustness, compensating for the channel fading and surrounding interferences. Secondly, the spatial multiplexing increases the data rate by serving users at different locations in parallel [3], offering efficient utilization of spectrum since all the users are still using the same spectrum band.

To utilize the advantages of massive MIMO concept, massive compact-size, and low-power-consumption RF front ends as well as the ability to accurately control each transmitted signal over the wide-band frequency range are required [4].

Since all the antennas in MIMO are working at the same frequency, the signal emitted by one antenna element can be coupled to another one due to the limited isolation level within antenna array. In a conventional communication system, circulators are inserted between antenna and PA to prevent the reflection from mismatch and mutual coupling. However, circulators are bulky, lossy and costly, especially when employed in a large number of RF chains. In addition, the removal of circulators enables the compact integration of RF front end. Based on these reasons, the next generation communica-

tion system will use circulator-free architecture, which invalidates some of the assumptions in conventional wireless communication architecture where circulators are used.

For example, PA and antenna designed for 50 Ohms with -10 dB return loss individually, will have at worst -5 dB mismatch when directly connected, which will cause severe power loss and linearity degradation and even damage the transistor. Furthermore, under the mutual coupling of the antenna array, a 50 Ohm-oriented PA is presented with a time-varying load modulated by signals from all the antenna elements, instead of its own physically loading antenna only. Since the impedance seen by the PA dictates the PA's performance, the varying load causes non-negligible nonlinear distortion.

In a wireless communication system, power amplifier is one of the most power-hungry components and dominates the total power efficiency in the system. Therefore, for ensuring a relatively high overall efficiency, PA is always driven into a high efficiency but more nonlinear region, which leads to a significant source of non-linearity. As the last stage of RF chain before antennas, PA has great impact on the transmitted signal quality. Especially in MIMO transmitter, non-ideality of PA's output directly generates the in-band and out-band distortion of the radiated signal, thus the beam-formed pattern and total channel capacity are degraded. Consequently, to fully understand the behavior of massive MIMO transmitters, the analysis methodology must be revised to take consideration of PA-Antenna interface at the presence of antenna finite isolation and PA mismatch [5]. For achieving this goal, a realistic PA-Antenna array system is a prerequisite, where all the nonlinearity are included and manifested, so that the comprehensive analysis can be conducted.

1.2 Problem statement

In SISO transmitter environment, especially for base station application, PA design is mainly focused on achieving high efficiency due to its decisive impact on the total efficiency of the chain, without intensive consideration of linearity. Then linearization techniques such as DPD, feedback, and feedforward, are applied to linearize the PA, which is operating in high efficiency mode but with nonlinear behavior. The gain of linearity is at the cost of additional power consumption and design complexity. When the power generated by single PA is over tens or hundreds of watts, this overhead is acceptable and cost-effective.

If the same PA design strategy is employed for MIMO transmitters, the system efficiency could be degraded significantly. The output power of each PA in a (massive) MIMO transmitter is scaled down with the increase of the number of PA. However, the DPD power consumption for each PA is still

kept the same when the load modulation problem is not considered. This way, the power consumed by DPD is already proportionally increased by the number of chains. It must be noted that the same multiple copies of PA designed for SISO transmitter working at MIMO scenario will experience load mismatch and load modulation induced from antenna coupling, as introduced by the thesis motivation in section 1.1. This issue motivates researchers to develop more complicated DPD schemes, like dual-input DPD [15] and multi-input DPD [7] to incorporate the couplings from other paths. The complexity of DPD further adds burden to the system or even becomes unfeasible in realistic hardware.

Therefore, the PA linearity issue needs to be examined specifically in MIMO scenario. This paper investigates experimentally the joint impact of RF power amplifier non-linearity and cross coupling between the antenna elements on the linearizability of sub-6 GHz digital beamforming arrays using SISO DPD technique. Specifically, it is shown that to avoid high complexity MIMO DPD both factors must be carefully co-designed. For example, highly nonlinear PA elements (e.g. -30 dB adjacent channel power ratio (ACPR) before DPD correction) would require very high isolation e.g. -30 dB between antenna elements (significantly in excess of the commonly assumed 20 dB isolation [12] [14], where the tested PAs are more linear, e.g. -40 dB ACPR before DPD correction), which may not be possible in practice especially for large array. This study thus demonstrates the importance of jointly designing the PAs and antenna arrays as separate designs cannot ensure overall system performance optimization. A 2 × 2 PA-Antenna array was designed, using GaN power amplifiers and patch antennas operating at 3.5 GHz, to serve as a device under test in the experiments.

1.3 Thesis Organization

This thesis is organized as follows. Chapter 2 introduces the PA nonlinearity and Digital Pre-Distortion to provide the background information. Then the literatures studying the antenna coupling effect in MIMO transmitters are summarized. From the literature review, the importance of employing the realistic RF front end to characterize the problem is demonstrated. The following is the thesis objectives. Chapter 3 and 4 presents the architecture of the designed PA and antenna array, and the reasons behind. The design steps are detailed, including the simulations and measurements. With the designed PA-Antenna array, system measurement and investigation is performed in Chapter 5. Different impact factors for SISO DPD performance in MIMO transmitters are studied. Enlightening design considerations for MIMO transmitter are given. At the end, the thesis is concluded in Chapter 6 and the future work is suggested.

Chapter 2
Background

The radio hardware imperfection degrades the transmitter performance. Among the components in RF chain, PA contributes the largest portion of nonlinearity, and impact significantly the total efficiency. In this chapter, the PA nonlinearity and SISIO DPD technique are introduced. Then the literatures of studying the PA nonlinearity behavior in MIMO transmitter are summarized.

2.1 PA nonlinearity

Among the various indicators for PA linearity, the AM/AM and AM/PM are the most widely used. AM-AM is power gain variation versus output power, and AM-PM is the output phase variation versus output power. These two curves are expected to be flat, which means the signal is proportionally magnified by the same magnitude amplification and phase shift. However, the real situation is illustrated in Fig.2.1 when stimulus is continuous wave (CW). The expansion or compression of AM-PM and AM-AM is the result of the variation of conduction angle and nonlinear parasitic capacitors of the transistor. The relatively flat part only exists at low power region, where PA operates less efficiently.

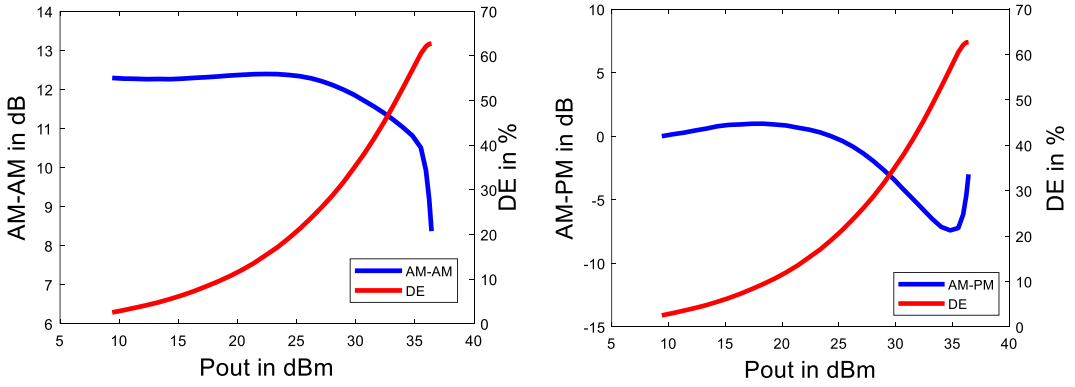

Fig.2.1 AM/AM and AM/PM vs. Drain efficiency (DE) of a Class AB Gallium Nitride (GaN) PA

In addition to the trade-off between PA efficiency and linearity, when the PA is driven by modulated signal, signal quality is also suffering from the dynamic distortion. Dynamic distortion is also known as memory effect because the PA output is a function of not only the current input, but also the past input. The memory effect can be caused by the frequency response of the matching network, the drain supply modulation due to the even term intermodulation product, and transistor properties

variation due to heat accumulation. Fig.2.2 depicts the dynamic distortion when a GaN PA is driven with a 100MHz OFDM signal.

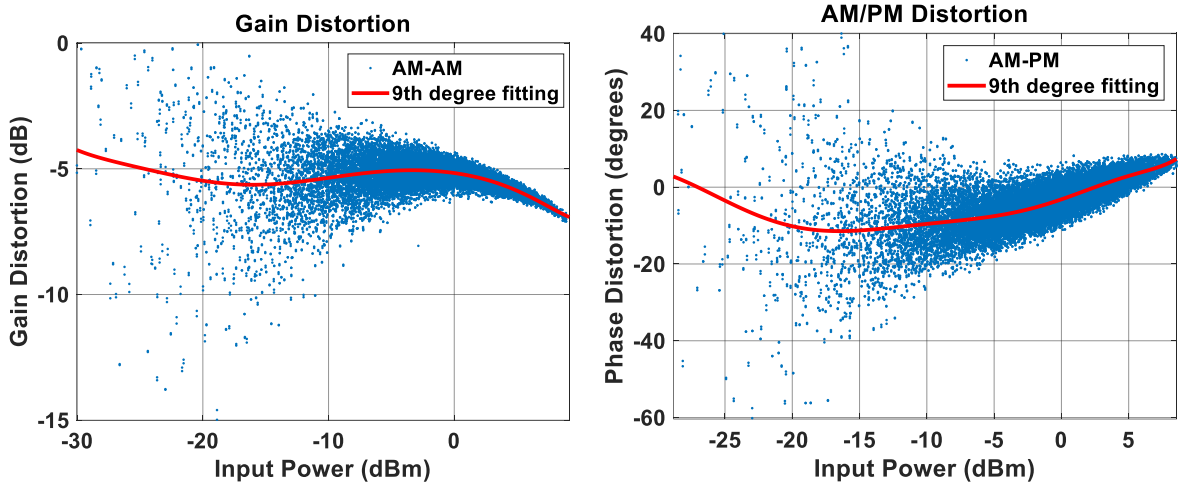

Fig.2.2 AM/AM and AM/PM of a GaN PA with 100MHz 8 dB PAPR OFDM signal

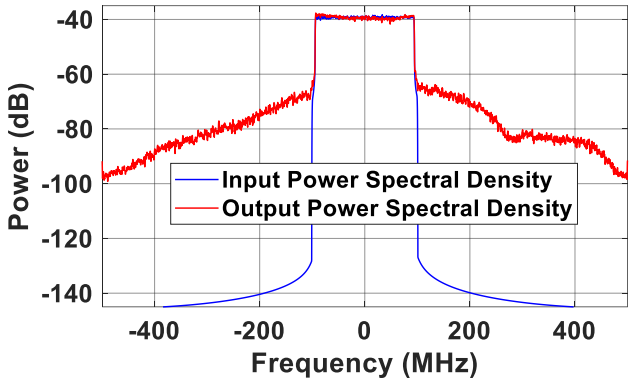

Fig.2.3 Spectrum regrowth and in-band distortion.

The consequences of the PA nonlinearity are the distortion of the transmitted signal and the leakage to the adjacent band as shown in Fig.2.3. The former deteriorate the signal quality, and the later generates interference to other channels. The deviation of the in-band signal is quantified by the normalized mean square error (NMSE), where $b(n)$ is the output signal normalized by the gain, $a(n)$ is the input signal:

$$NMSE = \frac{\sum_{n=0}^{N-1} |b(n)-a(n)|^2}{\sum_{n=0}^{N-1} |a(n)|^2} \tag{2.1}$$

The adjacent channel power ratio (ACPR) is used to evaluate the out of band distortion, where P_{adj} is the power of adjacent band, and P_{in} is the power of in-band:

$$ACPR = 10log\frac{P_{adj}}{P_{in}} \tag{2.2}$$

Both of these two factors need to be eliminated to as low as possible.

2.2 DPD technique

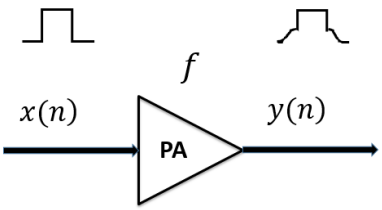

Fig.2.4 Block diagram of PA model

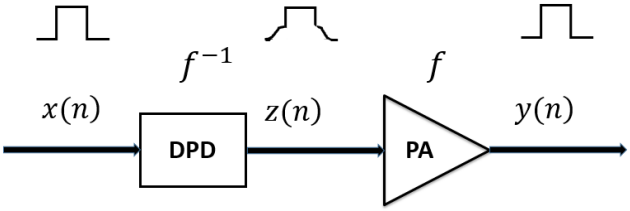

Fig.2.5 Block diagram of PA compensated by DPD

Digital Pre-Distortion has been demonstrated to be an effective way to pre-compensate the PA non-linearity. If a PA behavior can be described by a nonlinear function of input signal $x(n)$ with the output signal $y(n)$ as shown in equation (2.3) and Fig.2.4:

$$y(n) = f(x(n)) \tag{2.3}$$

The DPD applies the inverse function of f, f^{-1} before PA input such that the desired signal can be recovered at the PA output as shown in equation (2.4) and Fig.2.5:

$$y(n) = f\big(z(n)\big) \qquad z(n) = f^{-1}(x(n)) \tag{2.4}$$

Different behavior model functions and numerical solutions have been researched deeply and maturely. However, most of them are based on the single-input-single-output model, which means the PA behavior is only decided by the input signal. When applying SISO DPD to a MIMO transmitter, the expected linearization performance cannot be achieved because of the cross coupling between antenna elements, as the following section 2.3 and 5.2 will show.

2.3 Literature review on study of cross coupling effects in MIMO transmitter

Cross coupling is the signal leakage from other chains. In a conventional communication system, the cross-coupling normally exists between antennas: Antenna array has electromagnetic coupling between elements, which is linear in nature. In the meantime, isolators between PA and antenna protect the PA from the harm of load mismatch and injection of other signal. Thus the antenna coupling in conventional system only causes the linear distortion in output signals. Together with channel equalization, this linear coupling effect can be compensated at the receiver end easily. However, the future

generation communication systems will integrate massive transmitters in one chip or board, where shared LO, substrate and supplies introduce inevitable linear and nonlinear cross coupling effects [6]. In addition, the dense integration also requires the removal of isolators, which are bulky, lossy and costly. In an isolator-free architecture, the mismatch and coupling in PA-antenna interface needs special attention, because PA, a nonlinear device, will transfer the antenna linear coupling into a nonlinear problem when PA load is changing as shown in equation (2.5) and figure 2.6. The active impedance seen by PA is a function of all the incident signals and antenna parameters, which is the direct consequence of cross coupling. The cross coupling in a massive MIMO transmitter is complex and has significant effect on system performance. Great attention has been given to this topic during the past ten years.

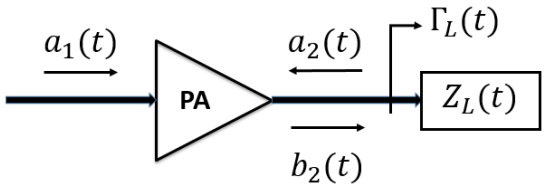

Fig.2.6 Active impedance embodied with reflection coefficient of the PA in MIMO transmitter

$$\Gamma_L{}^{(i)} = \frac{\mathrm{a_2}^{(i)}}{\mathrm{b_2}^{(i)}} = \frac{\sum_{k=1}^{k=N} \mathrm{b_2}^{(k)} \mathrm{S}_{ik}}{\mathrm{b_2}^{(i)}} \tag{2.5}$$

In 2009, the authors in [7] categorized the couplings into two groups, before PA and after PA. The couplings before PA are amplified and distorted by PA, which is the main source of nonlinearity of a transmitter. The conventional DPD is incapable of linearizing it because conventional SISO DPD is a function of single input signal. As for the coupling after PA, like antenna coupling, they claimed that this linear coupling can be easily compensated with the matrix inverse algorithm together with channel equalization, which is true for isolator added system. For simulation validation, they added the extra directional couplers before PA to create the RF nonlinear coupling, and provided the two branches with the same input signals. In their work, the transmitters' output with the effect of cross-talk is modeled as:

$$y_1 = f_1(x_1 + \alpha x_2) \qquad y_2 = f_2(\beta x_1 + x_2) \tag{2.6}$$

Fig.2.7 depicts the DPD architecture in this work. The proposed crossover-DPD is based on memory polynomial with the addition of input cross terms and formulates an approximation of the inverse of the composite nonlinearity in the two input two output transmitter, to linearize the distor-

tion introduced before PA. We can see from equation (2.6) and fig. 2.7 that it limits the study to the cross talk before PA in two-transmitter system, and only takes the linear combination of two inputs and ignores the higher order cross-terms. Besides, they didn't provide the measurement setup for validation of linear cross coupling effect.

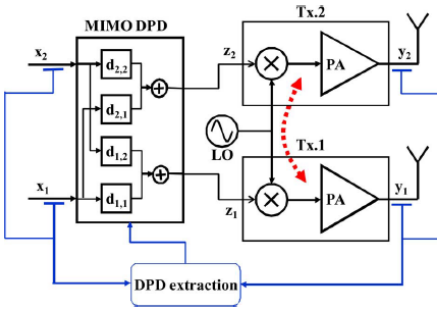

Fig.2.7 MIMO transmitter with crossover -DPD and nonlinear crosstalk [7]

Compared with [7], the authors in [8] conducted measurements not only for coupling before PA but also the coupling after PA. For quick validation and low cost setup, couplers before and after PAs are employed to artificially create coupling between signal paths. Again, they also believe the coupling after PA is linear combination effect. Respectively, Generalized Memory Polynomial for Nonlinear Crosstalk (GMPNLC) is proposed for compensating the coupling before PA as shown in equation (2.7) [8], and Generalized Memory Polynomial for Linear Crosstalk (GMPLC) is proposed for compensating the coupling after PA as shown in equation (2.8).

$$y_1 = f_1(x_1, |x_1|, |x_2|) + f_2(x_2, |x_2|, |x_1|) \tag{2.7}$$

$$y_1 = f_1(x_1, |x_1|) + f_2(x_2, |x_2|) \tag{2.8}$$

The couplers are inserted before and after PA to mimic the nonlinear and linear coupling effect respectively as shown in Fig.2.8 (a). For assumed linear-only coupling compensation, we can see the residue of out of band distortion by GMPLC is higher than that by GMPNLC, and similarly for the NMSE. This exactly demonstrates that the coupling at PA output is not simply a linear combination. Besides, their DPD architecture is multi-input based, i.e., a multivariate polynomial or Volterra series, which is already complicated for large number of signal paths, and not to mention that this high complexity calculation has to be done in every path of the transmitter.

These coupler-based simulations or measurements can only approximate two branch coupling cases, otherwise the complexity explodes significantly when considering all level of coupling in large antenna arrays. Therefore, the highest number of transmitter chain studied by means of couplers is

three in [9]. However, they put isolators closely behind PAs, and then followed by couplers. In this arrangement, the coupled signal doesn't feed the PAs because of the isolators, thus only linear coupling effect is studied, which is not realistic for 5G system.

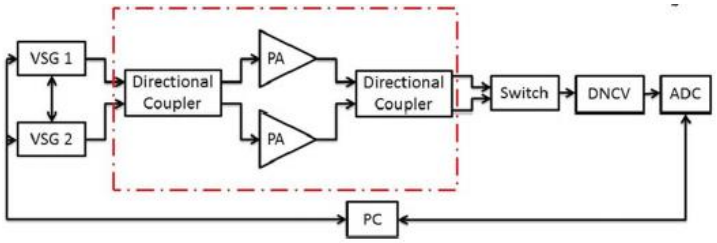

(a)

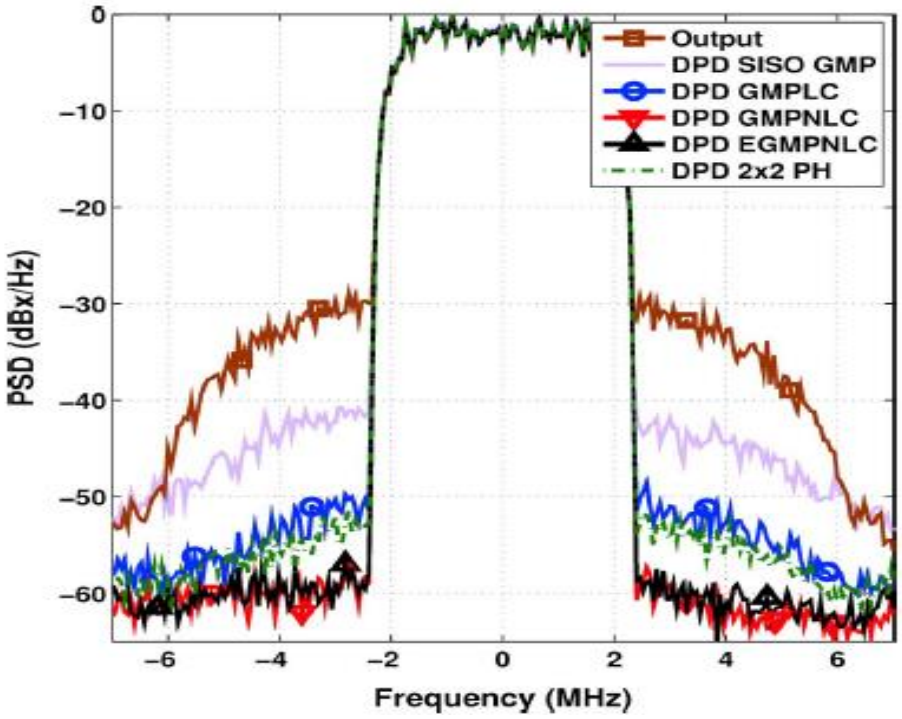

(b)

Fig.2.8 a) Measurement setup with different insertion of couplers b) measured power spectral density versus frequency for DPD of a device under test (DUT) with -20 dB linear crosstalk. The different inverse model used for DPD are explained in the legend [8].

Inspired by active load-pull system, direct injection of a signal into the PA output is another method to emulate the coupling effect in MIMO transmitter. For example, the work in [10] provided an antenna-free measurement setup as shown in fig.2.9. At the output of the DUT (PA), the second input

signal TX2, calculated based on RX1 and designated antenna parameters, is injected to emulate the power coupled from antenna. The circulator is placed for DUT matching. Since the signal injection change the effective load of the DUT, and thus DUT's output is also changed, the process is iterative. This setup works like an active load-pull, and it can emulate any level of coupling with any kind of adjacent input signals. According to their results, -20 dB coupling between two elements could avoid distortions by a large extent.

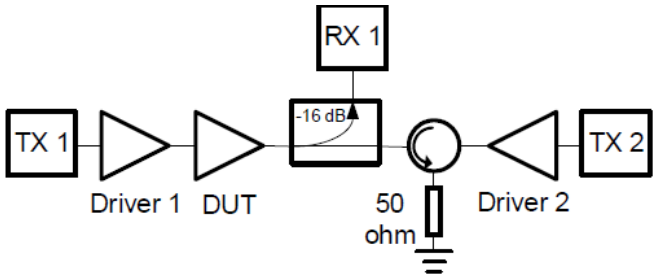

Fig.2.9 Proposed measurement setup for emulation of coupling effect [10]

Combing coupler and load tuner together, load mismatch and mutual coupling in MIMO transmitter are studied in [11] as shown in Fig 2.10. A unified behavior modeling and DPD solution is proposed to take into account of these two factors as a resultant reflection coefficient at the PA output. The reflection coefficient Γ_L is a function of active impedance Z_{in1} and Z_{in2}, which is determined by the physical part Z_{11}, Z_{22} and the virtual part $\frac{Z_{12}I_2}{I_1}$, $\frac{Z_{21}I_1}{I_2}$ as shown in the equation (2.9) [11]. The physical part embodies the load termination or mismatch, and the virtual part is led by the antenna coupling.

A set of training load points in the Smith Chart corresponds to different complex reflection coefficients. DPD coefficients are estimated for each point of the training load. The new coefficients for test load are generated from the interpolation of the training data with respect to the reflection, including both magnitude and phase. The model they used is a dual-input Memory Polynomial with the nonlinear order of crossover term [7] [8] between PA input and PA output reflection. For modeling extraction and validation, a programmable load tuner is added at the PA output to create mismatch, and an identical PA's output is coupled to the main PA output through a coupler to mimic the coupling from other paths. The inputs signals are limited to the two identical 20 MHz, four carrier Wideband code division multiple access (WCDMA) modulated signal centered at 2.3 GHz for main PA and coupling path PA. For Class AB PA and Doherty PA, the proposed Reflection-aware DPD can reduce ACPR by at least -13 dB and -10 dB respectively when mismatch and/or coupling exist. With

the same reflection magnitude but different angles, the modeling accuracy and DPD linearization performance vary significantly according to their results. It is worth noting that the excitation signals used for two paths are the same. Therefore the load variation presented is static within a given signal frame, which is just the load mismatch, not load modulation by the coupled signal at micron-second level. In essence, this work is still researching on the reflection-dependent crossover DPD.

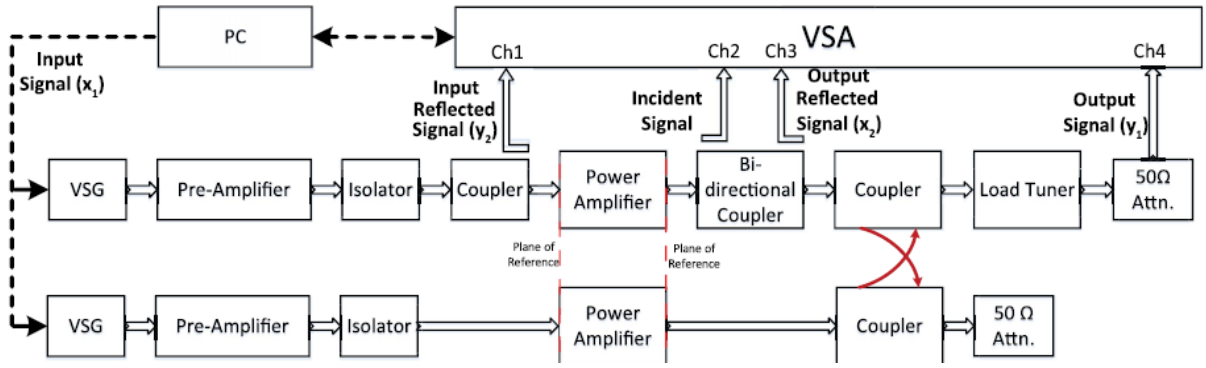

(a)

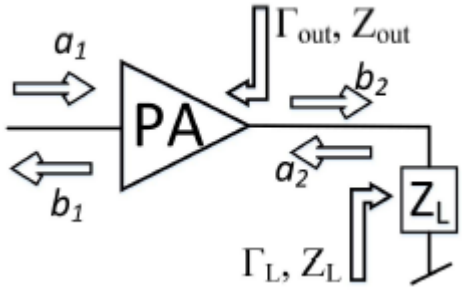

(b)

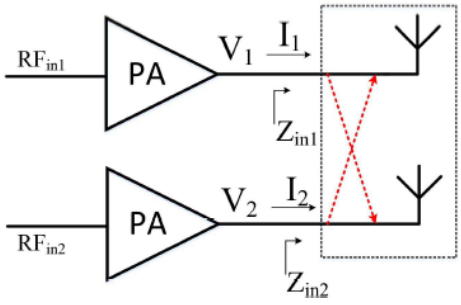

(c)

Fig.2.10 (a) Proposed measurement setup to emulating load mismatch and mutual coupling effect (b) Two-port power amplifier (c) Transmitting front end with mutual coupling [11]

$$\Gamma_L = \frac{a_2}{b_2} = \frac{Z_L - Z_{out}^*}{Z_L + Z_{out}} \qquad Z_L = Z_{in1} \text{ or } Z_{in2} \tag{2.9.a}$$

$$Z_{in1} = \frac{V_1}{I_1} = Z_{11} + \frac{Z_{12} I_2}{I_1} \tag{2.9.b}$$

$$Z_{in2} = \frac{V_2}{I_2} = Z_{22} + \frac{Z_{21} I_1}{I_2} \tag{2.9.c}$$

Instead of emulating the coupling effect in antenna array with extra couplers or load tuners, using real antenna array as load is more appropriate. The work in [12] did the investigation of two-branch PA and antenna array out-of-band distortion variation when having different antenna element spacing.

The setup is centered at 2.12 GHz and tested with two independent 5MHz WCDMA signals. The measurement shows that closer spaced antenna array introduces higher coupling and higher out-of-band distortion, which refuted that the assumption in [7] that antenna coupling only leads to linear distortion. And deterioration of the ACLR appears to increase proportionally in dB with the rising of antenna coupling. Based on dynamic extensions of the poly-harmonic distortion (PHD) model, the authors of [12] proposed a dual-input excitation PA behavior model in the low-pass equivalent complex envelope domain as shown in equation (2.10). $\mathbf{b}_2$, $\mathbf{a}_1$and $\mathbf{a}_2$ are vectors of the output and input waves for all N transmitter branches. $\mathbf{S}_{21}$, $\mathbf{S}_{22}$ and $\mathbf{T}_{22}$ are diagonal matrices containing the nonlinear parts of the PA function. And $\mathbf{S}_{ant}$ is the antenna S-parameter matrix.

$$\mathbf{b}_2 = \mathbf{S}_{21}(|\mathbf{a}_1|)\mathbf{a}_1 + \mathbf{S}_{22}(|\mathbf{a}_1|)\mathbf{a}_2 + \mathbf{T}_{22}(\mathbf{a}_1)\mathbf{a}_2{}^* \tag{2.10a}$$

$$\mathbf{b}_2 = \mathbf{S}_{21}(|\mathbf{a}_1|)\mathbf{a}_1 + \mathbf{S}_{21}(|\mathbf{a}_1|)\mathbf{S}_{ant}\mathbf{b}_2 + \mathbf{T}_{22}(\mathbf{a}_1)\mathbf{S}_{ant}{}^*\mathbf{b}_2{}^* \tag{2.10b}$$

Each power amplifier output is a nonlinear function of its input a_1 and the reflection combination a_2 from all the antenna ports at this PA output. The first item in 2.10 describes the PA nonlinearities, the second and third items describe the antenna mutual coupling and mismatch effects brought by antenna array. Unfortunately, this model does not predict the input impedance variations, and it also is a first order linear approximation, thus being still limited to relatively low levels of Voltage Standing Wave Ratio (VSWR).

Based on the similar dual input model in [12] mentioned above to predict the PA RF behavior in MIMO scenario, the authors in [13] also include the model of transistor DC current to predict PA efficiency and linearity properties under the MIMO environment. The transistor intrinsic current is transferred to the measured power supply current, by a low-pass filter composed of cable resistance and the largest decoupling capacitor as depicted in fig. 2.11 a). And the intrinsic dc current is decided by incident current and reflected current of the RF output. Thus the DC behavior model is based on the extraction of RF model. The PA model is extracted with OFDM signal (modulation bandwidth=20 MHz, PAPR= 10d B) at 2.1GHz using the active load-pull setup. The load variation range is confined in a circle on the Smith Chart, which is determined by a four by one linear dipole antenna array with -20 dB coupling level. Each PA is separately housed in metallic cover, and has its own PCB board. The system is measured in both phased array case, where highly correlated signals are used for excitation, and MIMO case, where totally different four OFDM signals are used. PA's efficiency, output power and ACLR show an evident variation when having different input phases in phased array scenario. Take PA efficiency as an example as shown in fig. 2.11 b). Besides, the addi-

tion of mutual coupling adds the imbalance to in-band signal spectrum and out-band regrowth comparing with the 50 Ohm termination case. The assumption they made is that all the PA are the same, thus the model extraction is done for one PA. However in reality each chain has inevitable hardware variations and would provide abundant diversity to the MIMO system, which may be taken advantage of since the diversity may offer a certain level of averaging cancelation in statistics. Proper DPD probably is able to correct the linearity degradation, but cannot do anything with output power compensation.

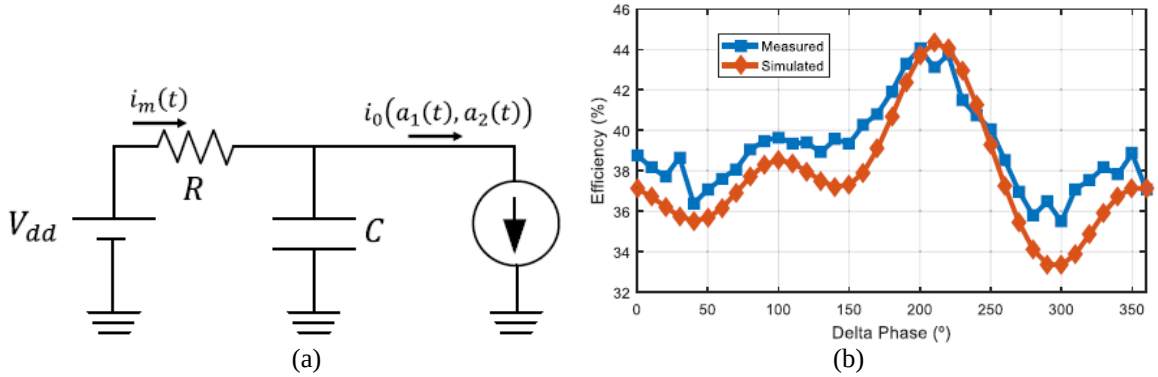

(a) (b)

Fig. 2.11 a) Equivalent model for the dc current generation. b) simulated and measured PA behavior when having different input phases.[13]

An antenna array closer to real application in 5G base station is employed to study the coupling effect in [14] and [15]. The two by two microstrip patch antenna array is a typical array that incorporates the three kinds of coupling level between four elements, which offers the flexibility to test different input combinations. As an extension of work in [12], a dual-input Volterra series-based model is pruned to a dual-input memory polynomial model, which includes PA nonlinearity and its mixing terms with mutual coupling and mismatch [14]. Besides, for non-flat frequency response antenna array, finite impulse response (FIR) filters, derived from multi-frequency S-parameters, are used to describe the relation between an incident wave and the output signals, instead of using single frequency S-parameters. They designed a high coupling level (-12 dB) and a low coupling level (-24 dB) two by two antenna arrays. Four different and independent 20MHz OFDM signals with 8.5 dB PAPR are used for driving the four PAs. The model were used to predict the behaviors of single PA and PA array with and without SISO DPD as shown in fig.2.12. Based on their results, we have the conclusion that the distortion due to mutual coupling and mismatch are lower than the distortion of the PA itself, but cannot be linearized by SISO DPD, especially in a high coupling environment.

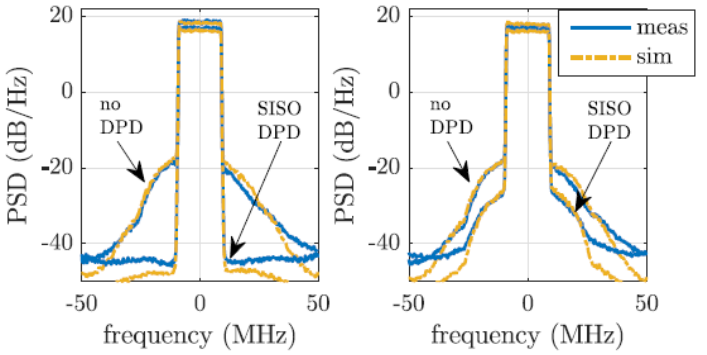

(a)

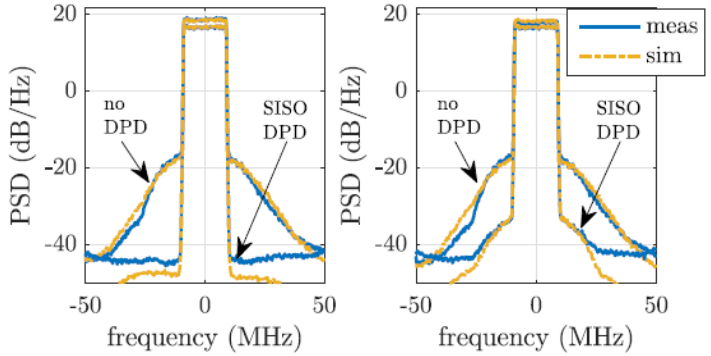

(b)

Fig. 2.12 Spectra of PA1 for (a) high-coupling array and (b) low-coupling array. Left: PA is operated in a single-path scenario. Right: MIMO scenario. Measurements (meas) without SISO DPD and with SISO DPD are compared with simulations (sim) without SISO DPD and with SISO DPD [14]

Later on, a DPD solution is proposed for MIMO transmitter to linearize the distortion due to antenna mutual coupling and mismatch in [15], avoiding the complexity explosion for large number of antenna array. The DPD architecture can be divided into two parts: a linear relationship which describes all the inputs and output of an antenna array, and is shared by all the parallel channels depicted by CTMM (crosstalk and mismatch model) block in Fig. 2.13; and a nonlinear dual-input DPD block, originating from the model in [12], that exists at each transmit path, as shown in Fig. 2.13.

Since the complexity of CTMM block is linearly increasing with the number of transmitting paths, and dual input DPD of each path has nothing to do with the total number too, the complexity does not explode when scaling up the transmitting paths. Yet the performance achieved by this technique is extremely similar to the multi-input DPD, which has significantly coefficients explosion for large MIMO system. A single antenna is placed at far field to measure the combined signal. The ACPR

improvement of the combined signal is close to the improvement of individual PA. However, the signal bandwidth is limited to only 5MHz, which does not satisfy the requirement of the next generation communication. For calculating CTMM coefficients, they made an assumption that the PA output $\mathbf{b}_{2k}(n)$ already equals the desired input signal $\mathbf{b}_{dk}(n)$, which corresponds to the linearized scenario. This might not be an accurate estimation. In addition, the PA used to predict the behavior in [14] and verify the DPD performance in [15] are four SKY66001-11 amplifiers, which are linear amplifiers and not representative application for base station.

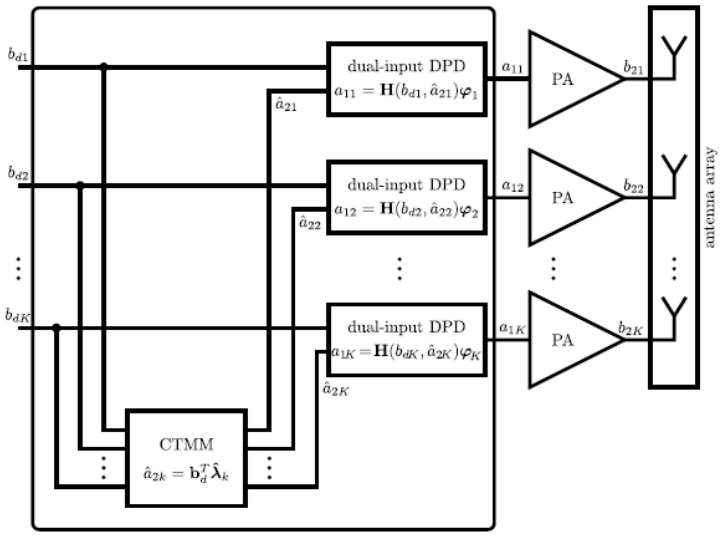

Fig. 2.13 Block diagram of a multi-antenna transmitter with the proposed DPD method [15]

To get a better analysis of PA nonlinear distortion caused by antenna array coupling, the numerical simulation for a 64-element PA-Antenna transmitting array was conducted in [16]. Using circuit envelop simulation with 5 MHz WCDMA signal, the PA model is extracted based on the two-input behavior model in [12] for memoryless case. The active impedance, a_2 / b_2, shows an evident variation space when the antenna array is steered for different angles. The central elements in array experience severer changes than the ones on the edge. Accordingly, the PA nonlinear properties embodied as AM-AM and AM-PM also display the dependence in the element location and beam angle. It should be noted that at certain beam angles, AM-AM curves have different expansion and compression level as shown in Fig.2.14, which provides the possibility of canceling each other at the combined signal (The relevant simulation is done in [17]).The PA inputs have the same signal magnitude with different phases, which corresponds to the phased array case. However, in a more general scenario, e.g.

digital beamforming, all inputs are totally different at magnitude and phases, which could present larger impedance variation in the Smith Chart and even negative impedance.

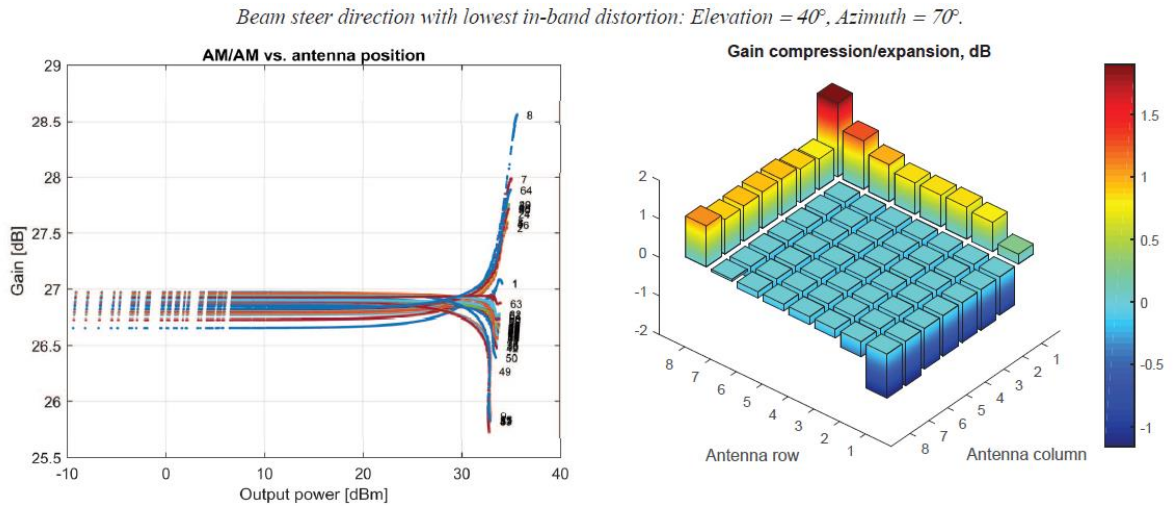

Fig.2.14. Simulated AM/AM distortion in each of the 64 transmitter PAs. Contour plots to the right show maximum dB deviation from constant gain. [16]

2.4 Thesis objectives

From the review and analysis above, it is significantly necessary to build a two by two PA-Antenna array system, where all the nonlinearity is included and manifested so that the comprehensive analysis can be conducted. For fulfilling this purpose, employing typical PAs and antennas for 5G digital beamforming base station with wideband signal verification is the prerequisite to reveal the sources and mechanism of nonlinearities in realistic MIMO system. Firstly, the antenna gain and PA output power decide the equivalent isotropically radiated power (EIRP), which describes the transmission power in a certain direction. Consequently, those low power linear PA for cellular application should not be used as device under test in this investigation. Besides, wider bandwidth transmitter can provide higher system capacity, which is highly desired in 5G system. As for the antenna array isolation, there is no meaning to deliberately create a high coupling array, e.g. placing elements closer than λ/2, because this arrangement will harm the antenna radiation pattern, leading to nulls in the coverage region, and also exaggerate the load variation level induced by antenna coupling. Last but not least, since the distortion and linearizability of PA array under finite antenna coupling is the subject of this thesis, each PA alone should be linearizable when working separately, such that the impact of antenna cross coupling can be isolated from the impact of nonlinearity of PA. Based on the analysis above, the

design specifications are given. Up to date, no literatures have been found in investigating the PA load modulation problem with such realistic hardware system.

The power, efficiency, bandwidth, and linearity requirements of the PA in this thesis for OFDM signal transmission are as follows:

- Average output power > 25dBm under modulated signals with PAPR of 8 dB
- Peak Drain Efficiency (DE) > 50% across the band
- Fractional Bandwidth (FBW) > 15%
- Adjacent channel leakage ratio (ACLR) < –45 dB after DPD linearization
- Normalized mean square error (NMSE) < 3%.

Antenna bandwidth, gain and isolation specifications are given:

- Fractional Bandwidth (FBW) > 10%
- Array broad side gain >11 dB
- Array isolation > 20 dB

Chapter 3
Antenna array design

Building MIMO RF front end is complex and costly, thus plenty of work on MIMO transmitter only uses several identical commercial PAs combined by couplers and loaded with load tuner to emulate the complicated mutual coupling effects and active load variation [9] [11] [18]. However, this emulation does not represent the realistic load modulation situation. First, the artificial coupling created by couplers only emulates the magnitude of S_{ij}, yet the phase of S_{ij} decides the constructive or deconstructive impacts of the combined waves, which, together with magnitude, determine the active impedance seen by the PA. Second, antenna elements at different locations experience difference coupling level and combination. For example, the Fig.3.1 displays a 16-element antenna array with different levels of coupling. For the element sitting in the center, they have four highest coupling paths, four less strong coupling path and other weak coupling paths. On the contrary, the corner antennas have only two highest coupling and one less strong coupling. Hence only using several couplers is not comprehensive to embody the various physical coupling.

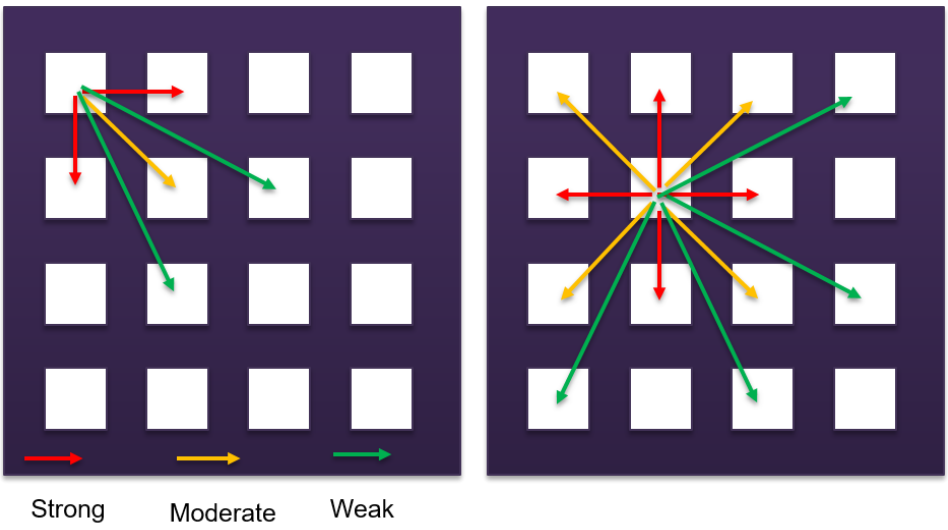

Fig.3.1 Antenna array showing different coupling levels

Furthermore, the passive load tuner is unable to provide microsecond-level load variation, which is the envelop variation time scale. Thus the passive load tuner can only emulate load mismatch instead of load modulation for PA. In conclusion, in order to investigate the active load modulation in MIMO system, a real antenna array is unavoidable.

Although [13] used real antenna array for their test, the linear array, again couldn't stand for the complete real antenna array coupling case. Besides, [14] had two by two patch antenna array, but narrow matching bandwidth limits the measurement with wideband signals. Wideband signal test reveals more details of PA memory effect when operating in such active load modulation environment. So it is imperative to design a real 2D antenna array with wide bandwidth.

3.1 Single wideband antenna

A two-layer microstrip patch antenna is designed.

Microstrip patch antenna has been attracting attention for the past 50 years for its low profile, low cost and easy to integrate with other printed circuit. Especially in MIMO system, planar property of patch antenna makes it possible to integrate with PA closely in the same panel as will be shown later in chapter 4. In the meantime, the wide beam width of path antenna allows better beamforming coverage. However, the plain microstrip patch antenna is a resonator, which has narrow band characteristic by nature (less than 10%). In order to perform more comprehensive measurement related to memory effect, we need to increase the operation bandwidth of the signal, and the matching bandwidth of the antenna as well. Accordingly efforts have been made for enlarging the bandwidth of microstrip patch antenna.

Basically, the bandwidth of patch antennas can be broadened in two ways. One way is to increase the substrate thickness and decreasing its dielectric constant. Both reduce the Q factor of the resonator. The second way is to introduce multi-resonance to the radiator and align resonances closely. Because of the single-resonance nature, bandwidth improvement by tuning the substrate is limited. Based on the theoretical analysis in [19], for larger than 10% bandwidth, the ratio of substrate thickness over λ_g (wavelength in substrate) has to be at least 0.1, which imposes restriction for feeding structure. As to the second approach, investigation and design are intensively conducted. For example, adding parasitic elements above the main patch [20] or around the main radiator [21], cutting the U-shape [22] or V-shape slot [23] on the patch to introduce a second or third resonance. A non-radiating resonant created by L-shape feeding probe [24] can be used to modify the input impedance of antenna so as to increase the bandwidth. Besides, adding shorting pin [25] to excite and merge more than one modes [26] simultaneously are also quite helpful for bandwidth extension.

Among all the techniques mentioned above, two-layer stacked patch antenna is simple to design and fabricate, easy to be scaled to an antenna array and able to provide a reasonable wide bandwidth for our investigation (above 10%).

A stacked microstrip patch antenna consists of more than one metallic patch layers. Layers are electromagnetically coupled between each other. As shown in the fig 3.2, the top patch is the radiating element, coupled from the bottom patch, which is feed by a coaxial connector backward. The bottom patch introduces the second resonance. By proper tuning the distance and dimensions of two patches, the two resonances can be merged closely to form wide impedance bandwidth. Particularly for the air substrate case, works in [27] found that the wide impedance bandwidth happens at the air gap smaller than λ/10.

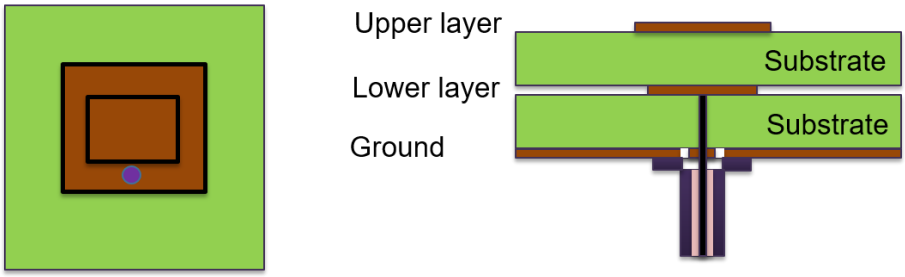

(a) (b)

Fig 3.2 Top view (a) and side view (b) of two layer antenna

3.1.1 One layer antenna

Design starts from a one-layer patch antenna, centered at 3.5 GHz. A 22.66 mm by 20.6 mm metal is etched on Rogers 4003C substrate, which is composed of two standard 60 mil Rogers 4003C laminates and a 4 mil RO4450F bondply. A conductive via feeds the antenna from ground layer to patch layer. The antenna is excited by a 50 Ohm coaxial SMA connector, accounting for the discontinuity from the coaxial cable to the feeding position. Fig. 3.3 depicts the top and side view of the one layer antenna. The full Electromagnetic (EM) simulation is performed in ANSYS HFSS.

As expected, one-layer patch antenna only has 3.4 % fractional bandwidth as the simulated S-parameter showing in the Fig.3.4. At the center frequency 3.5 GHz the maximum gain is 7 dBi.

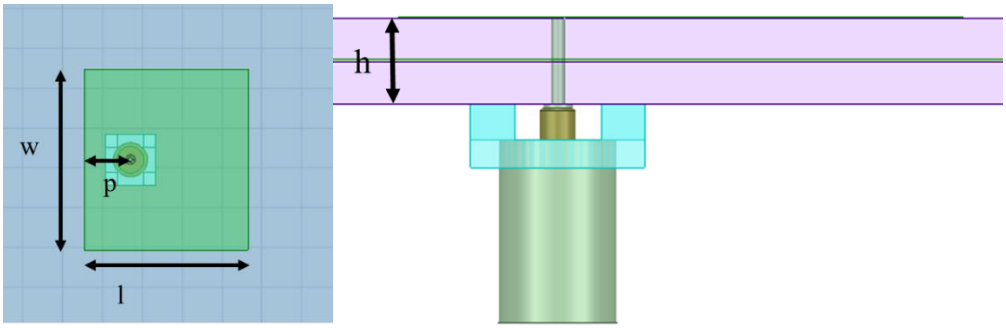

Fig. 3.3 Top (left) and side view (right) of the one-layer antenna. w=22.6 mm, l=20.6 mm, p=5.8 mm, h=124 mil.

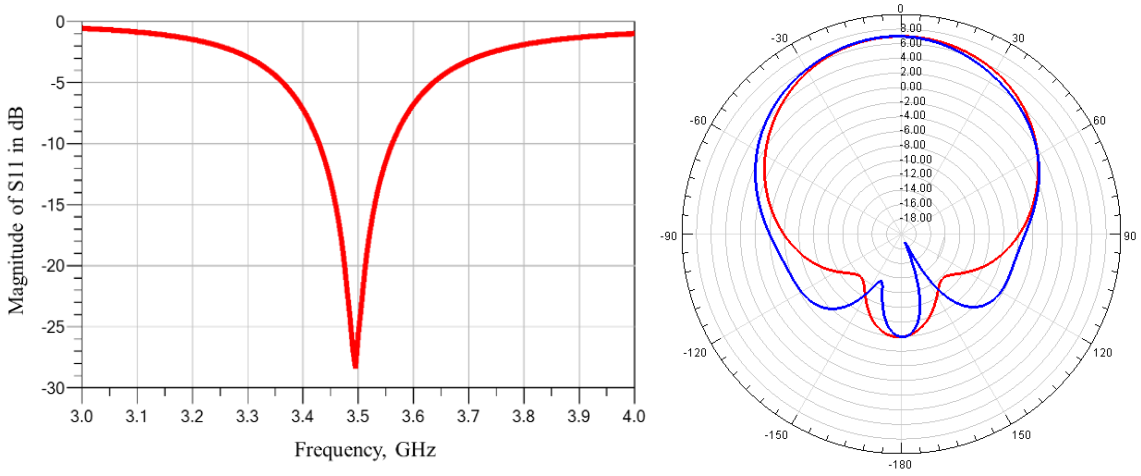

(a) (b)

Fig. 3.4 Simulated S-parameter a) and radiation pattern for phi=0 (red) and 90 degree (blue) b) of the single-layer antenna

3.1.2 Stacked microstrip patch antenna

In order to improve the impedance bandwidth, the parasitic layer is added as shown in Fig 3.5. Considering the ease of fabrication, the same substrate stack-up for the parasitic patch is used and the two parts are assembled together. Dimension details can be seen from Fig.3.5. The ground panel size is 55 mm × 55 mm.

From the return loss plot of two layer stacked antenna shown in Fig. 3.6, two resonance frequencies, 3.48 GHz and 3.62 GHz, can be recognized clearly. The peak gain at 3.5 GHz is 7.1 dBi. From 3.3 GHz to 3.7 GHz, the return loss is less than -10 dB. The fractional bandwidth is around 11%

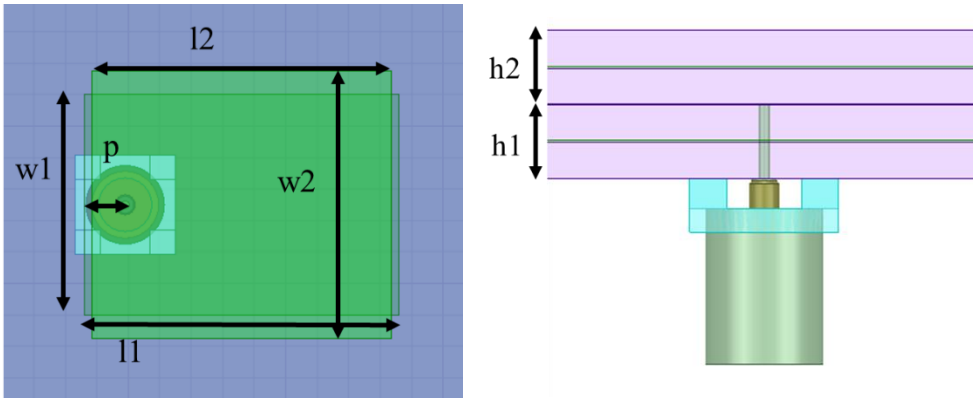

Fig. 3.5 Top (left) and side (right) view of Stacked Microstrip patch antenna. Lower patch w1=14 mm, l1 = 20 mm, p=2.6 mm, h1=120 mil. Upper patch w2 = 17 mm, l2 = 19 mm, h2 = 120 mil.

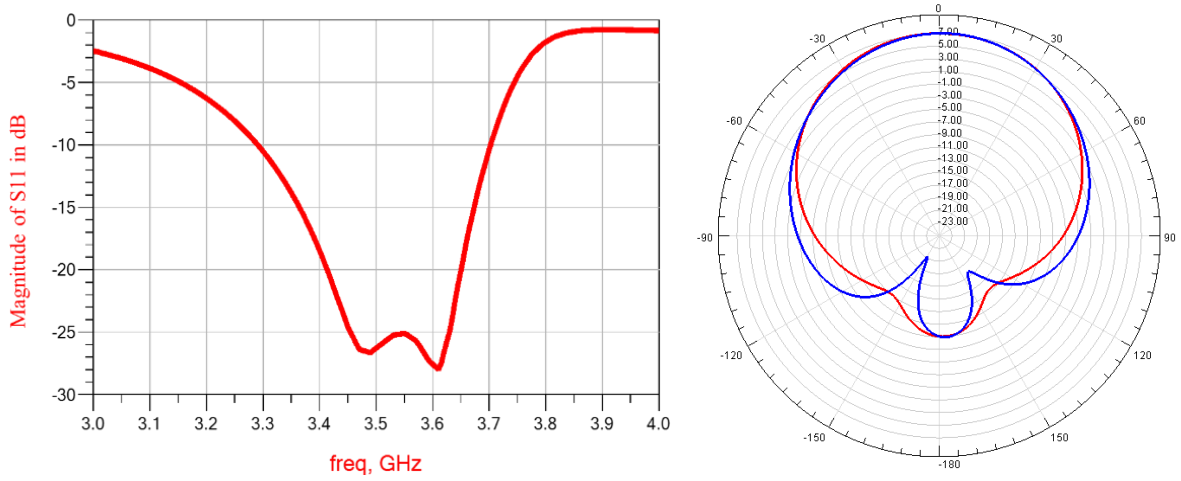

(a) (b)

Fig. 3.6 Simulated S-parameter a) and radiation pattern for phi=0 (red) and 90 degree (blue) b) of the stacked antenna

3.2 Wideband high isolation antenna array

As analyzed in Chapter 2, if a perfectly isolated antenna array is used, the load variation caused by mutual coupling will be eliminated in essence. Mutual coupling reduction technique for multi-antenna system is an active research topic for the past twenty years. Decoupling networks [28] and neutralization lines [29], introducing extra signal coupling at the inputs of antennas, cancel the original mutual coupling between two antennas. But the network only deal with the coupling between two ports, and it's difficult and complex to extend the two-port network to a multi-port 2D network. Defected ground structures [30] , etching different shape of slots in ground metal, cut the surface current flow

induced from coupling, yet the backward radiation may be increased due to the slot leakage. Electromagnetic bandgap (EBG) [31] structures or metamaterials [32] take advantage of the band stop characteristics in their frequency response to prohibit the coupling between adjacent antennas. However, their periodic structure, and the complicated design parameters, pose large space requirement and design complexity.

Inserting parasitic elements [33] between antennas to suppress the surface current from one antenna to another is a space-saving and low-cost approach to reduce mutual coupling. But how to make the suppression effective for wideband is not straightforward. B. Lakshmi Dhevi and all proposed an asymmetric loop resonator in [34]. This asymmetric loop provides two different paths for surface wave to cross from one side to the other, ending up with different phase delay and canceling each other as shown in Fig.3.7 (a) [34]. The loop is modified with the addition of a capacitive microstrip line, which widens the suppression bandwidth of the resonator further as shown in Fig.3.7 (b). The loop resonator in Fig.3.7(b) [34], acting as a band stop filter as shown in Fig.3.8 [34], is employed for the two by two antenna array design in this thesis.

Each element is the single wideband antenna designed in the last section and the center to center distance is λ /2 (λ here is the wavelength in free-space for center frequency 3.5 GHz), which is the realistic spacing for beamforming application. The two loop resonators are etched between antenna 1, 2 and 3, 4 on the same layer of upper patch, going along with the E plane as shown in the Fig. 3.10. For patch antenna, the coupling parallel with the length is E plane coupling, which is dominated by electric field, and the coupling perpendicular to E plane is the H plane coupling, dominated by magnetic field. The loop resonators can be used to block the H plane surface wave between antenna 1 and 2, however based on the simulation, the loop resonator doesn't help to reduce the E plane coupling. Thus only one direction decoupling elements are added. The dimensions of the loop in Fig. 3.9 are the following: w_1= 2.3 mm, l_1= 40.4 mm, w_4 = 0.5 mm, l_3 =34.6 mm, w_2 = 0.3 mm l_2 = 11 mm, d = 3.4 mm.

The S-parameters and radiation pattern with/without loop resonators are plotted in Fig. 3.11. Without the loop resonator, H plane coupling S_{12} and E plane coupling S_{13} are both around -17 dB. With the addition of loop resonator suppressing H plane coupling, S_{12} is reduced to -21 dB for the entire band. For the other direction, S_{13}, remains to be -18 dB ~ -19 dB. The radiation pattern in H plane, shown in blue curves in Fig. 3.11 (d), is also affected by the loop resonators and has a little narrower beam width than that without loop resonators in Fig. 3.11 (c).

(a) (b)

Fig. 3.7 Evolution of the decoupling unit cell [34]. (a) Asymmetric loop resonator with different loop lengths. (b) Wideband loop resonator proposed by [34]

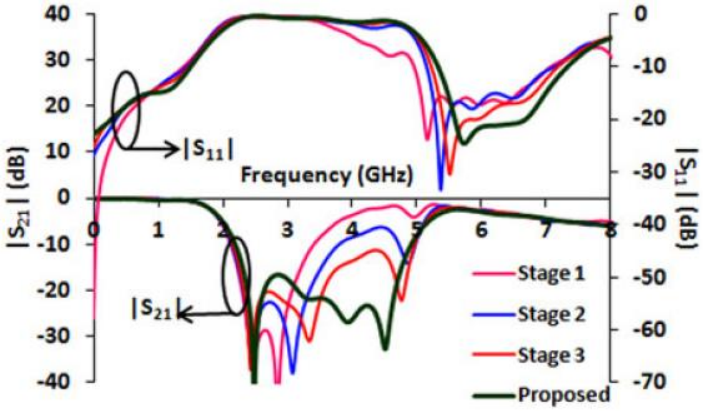

Fig. 3.8 S-parameter characteristics of the loop resonator (Stage 3 corresponding to Fig.3.7a, Proposed corresponding to Fig.3.7b) [34]

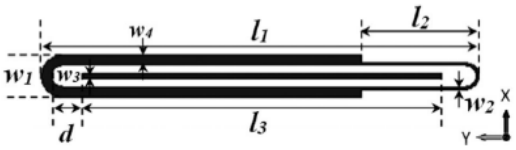

Fig. 3.9 Loop resonator dimensions

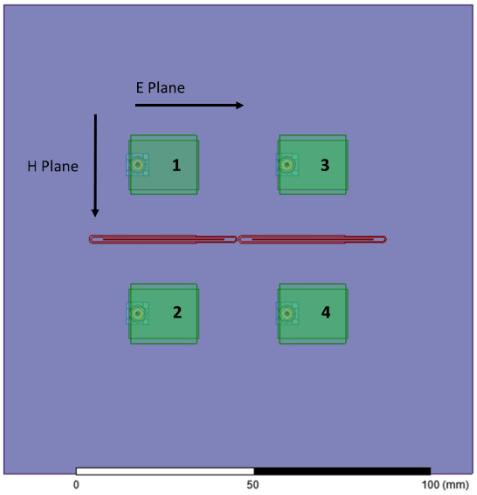

Fig. 3.10 Top view of two by two antenna array with loop resonators

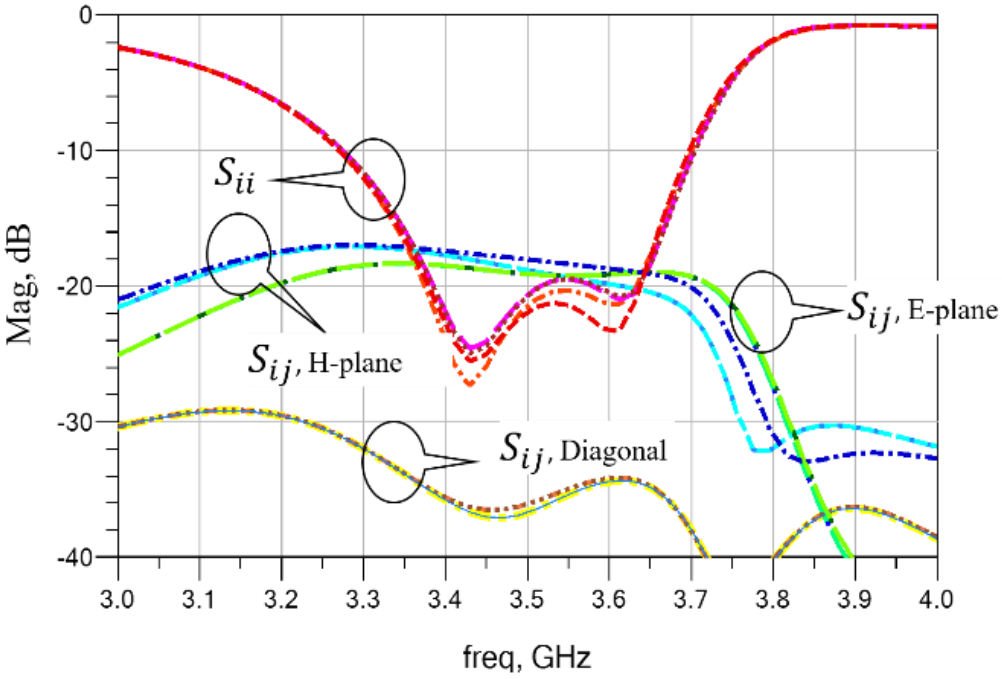

(a)

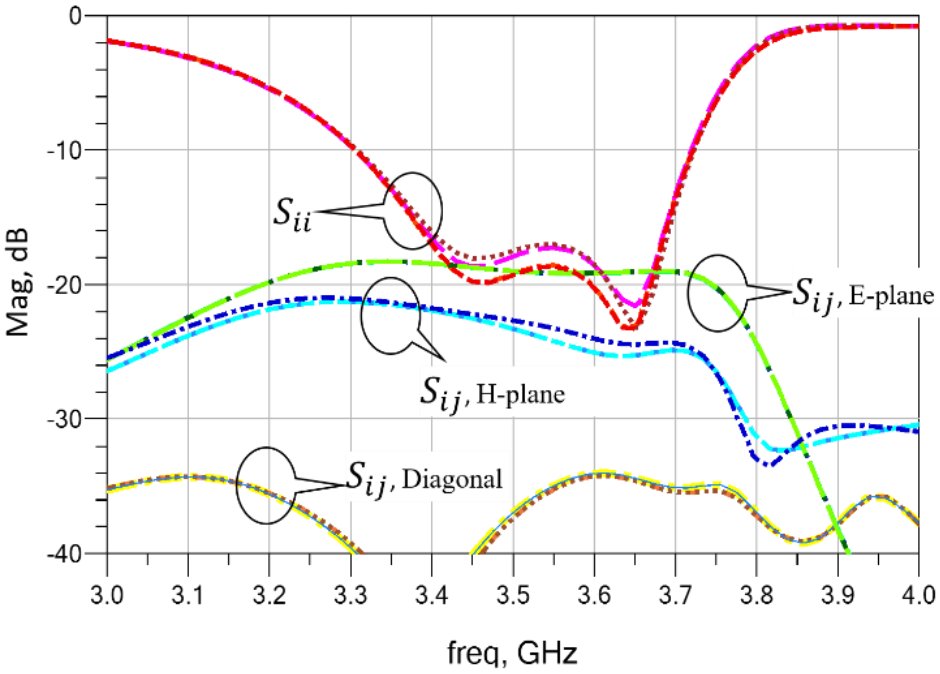

(b)

Fig. 3.11 (a) Simulated S-parameters without loop resonators b) Simulated S-parameters with loop resona-tors. c) Simulated radiation pattern without loop resonators for phi=0 degree (red) and 90 degree (blue).d) Simulated radiation pattern with loop resonators for phi=0 degree (red) and 90 degree (blue).

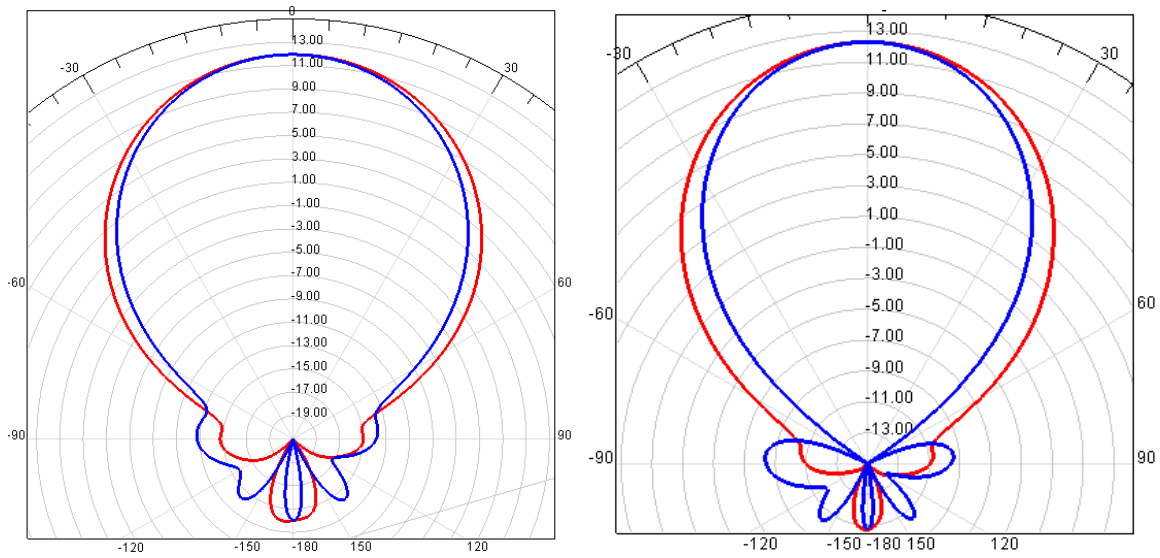

(c) (d)

As continue of the last page. Fig. 3.11 (a) Simulated S-parameters without loop resonators b) Simulated S-parameters with loop resonators. c) Simulated radiation pattern without loop resonators for phi=0 degree (red) and 90 degree (blue).d) Simulated radiation pattern with loop resonators for phi=0 degree (red) and 90 degree (blue).

With the same design methodology but different substrate stack-up as shown in Fig,3.12 (a), a wider bandwidth and higher isolated two by two antenna array is designed and simulated in HFSS. The simulated S-parameters are plotted in Fig.3.12(b). From 3.4 GHz to 3.6 GHz, the designed array has -28 dB isolation level. However, due to the high fabrication cost of Rogers 5880, only the initial design based on RO4003C is fabricated.

In digital beamforming scenario, each RF chain has significantly different signal magnitude and phase. Therefore, the active impedance plot should embody this application scenario. In Fig. 3.13, the active impedance variations of low isolated array and high isolated array are plotted on the Smith Chart from 3.3GHz to 3.7GHz when input phase for element 1 2 3 and 4 are 0, 20, -50, 79 degrees respectively. The maximum input stimulus power ratio between elements are set to 0 dB (phased array scenario, all chains have the same signal magnitude), 10 dB, 20 dB and 30 dB. For comparison, the passive reflection coefficients of one element of the array (since all four elements are the same) is also plotted in black. The other four colored curves are active impedances of the two arrays of each input. It's clearly seen that higher power difference between antenna elements leads to larger expansion in Smith Chart. With high power difference or low isolation level, negative impedance may appear as shown Fig.3.13 (e), (g), and (h). Improving isolation of the antenna array reduces the active

impedance variation. From the point view of investigating load modulation, a highly isolated antenna array is incapable to manifest the nonlinearity issue, which usually happens in a normal antenna array. Thus the low isolated antenna array is fabricated and used as the device under test.

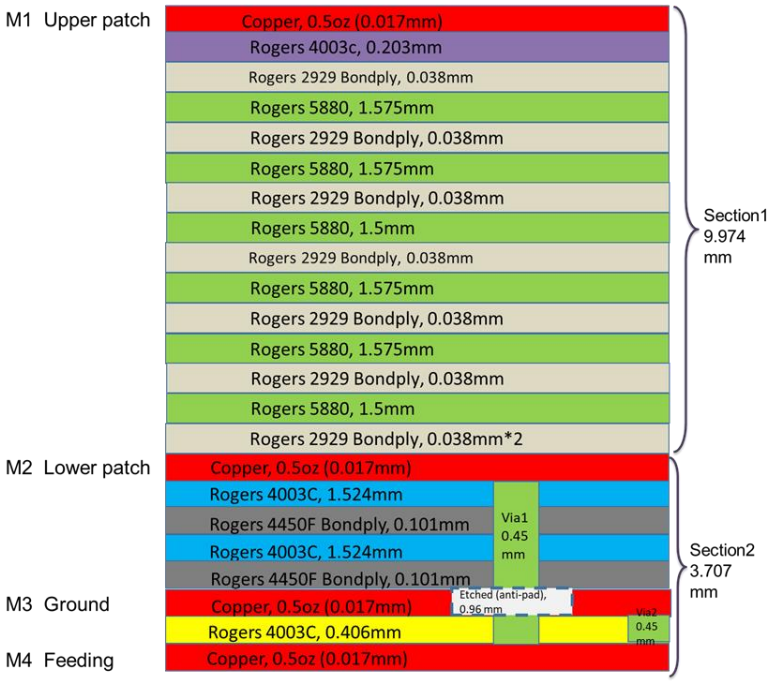

(a)

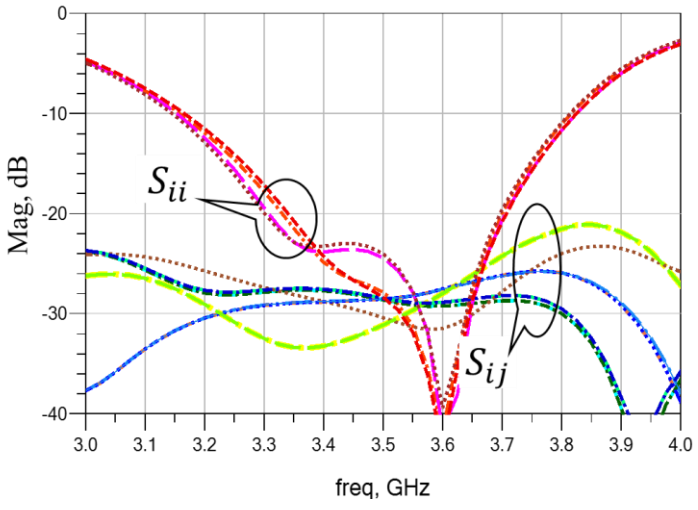

(b)

Fig. 3.12 (a) Rogers 5880 stack-up for highly isolated array (b) S-parameters of highly isolated antenna array

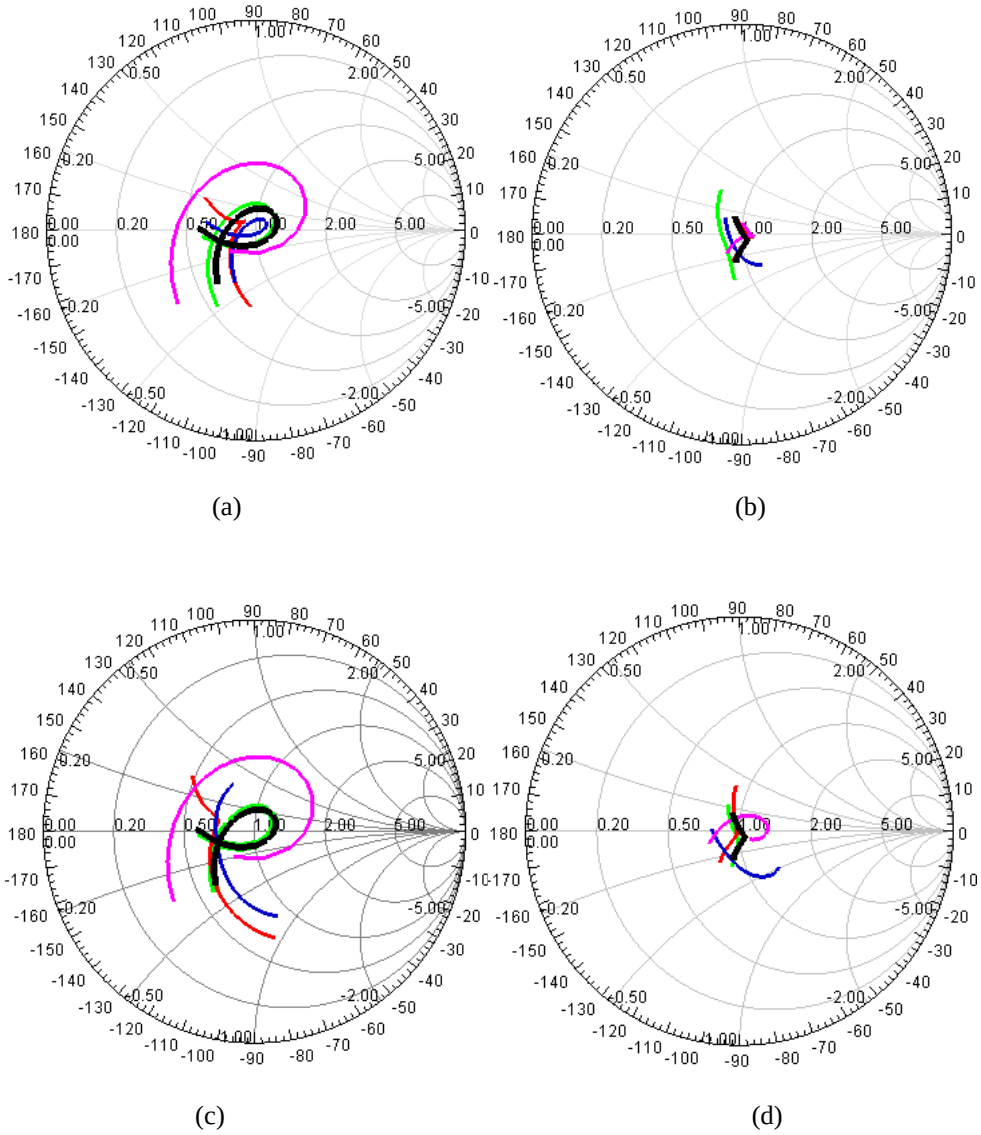

(a) (b)

(c) (d)

Fig. 3.13 Active S-parameters and passive S-parameters of low isolation array (a, c, e, g) and high isolation array (b, d, f, h) for different power ratio of input stimulus: 0 dB (a, b), 10 dB (c, d), 20 dB (e, f) and 30 dB (g, h). Black curves are passive impedance of the antenna element; colored curves are active impedances of each element.

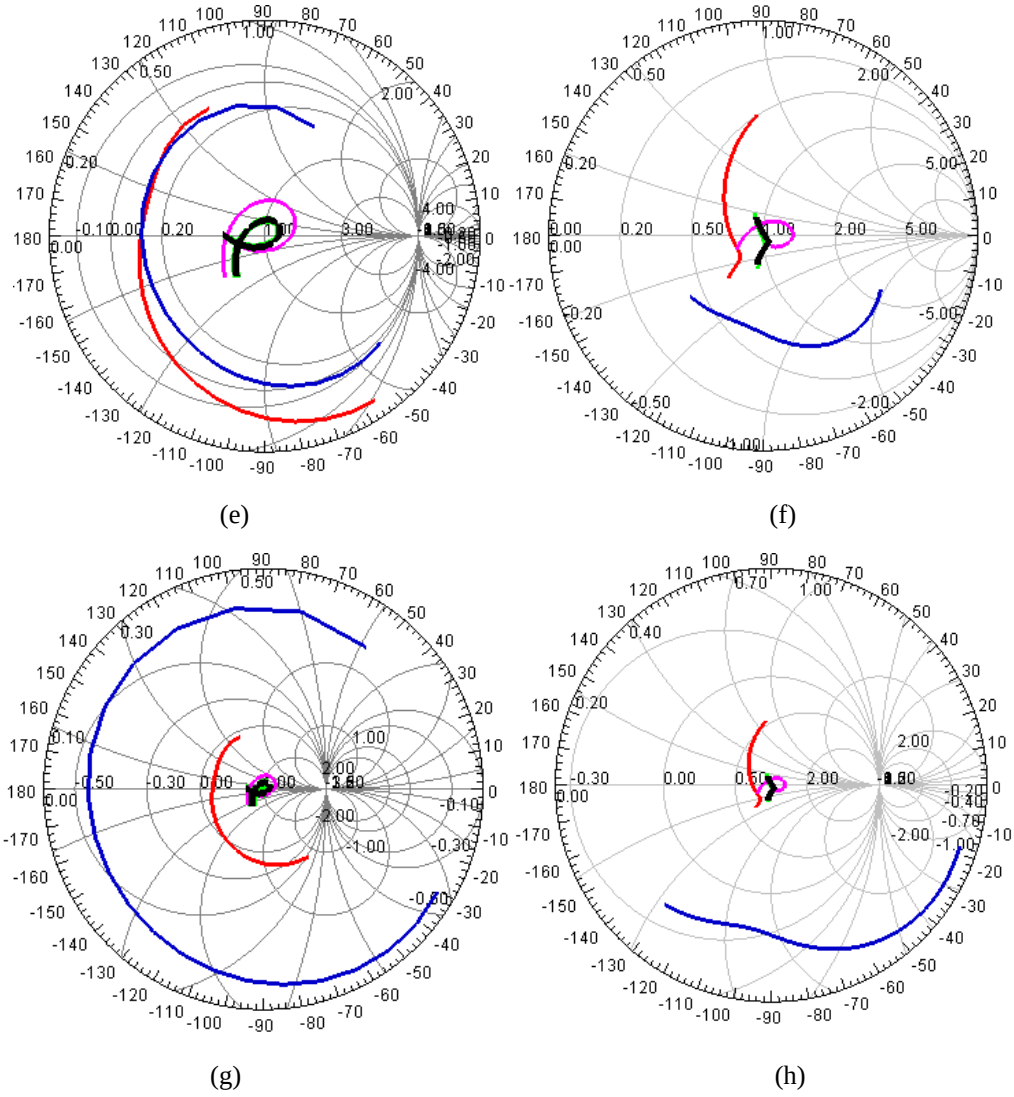

(e) (f)

(g) (h)

As continue of the last page. Fig. 3.13 Active S-parameters and passive S-parameters of low isolation array (a, c, e, g) and high isolation array (b, d, f, h) for different power ratio of input stimulus: 0 dB (a, b), 10 dB (c, d), 20 dB (e, f) and 30 dB (g, h). Black curves are passive impedance of the antenna element; colored curves are active impedances of each element.

3.3 Antenna measurement

Picture of the antenna and test environment is shown in Fig. 3.15. One element antenna and antenna array measurement are given in Fig. 3.14 and Fig. 3.16 respectively. Comparison between measurement and simulation of one element of antenna array is displayed in Fig.3.17. A frequency shift is observed for S_{ii} in the comparison between simulation and measurement in Fig.3.14 and 3.17, which is caused by manufacturing deviation of dielectric constants. The measured S_{ii} shows wider band-

width in terms of input matching, which is due to the loss of substrate, connector and cables. However, the estimated coupling level is quite consistent with the measurement as shown in Fig. 3.17.

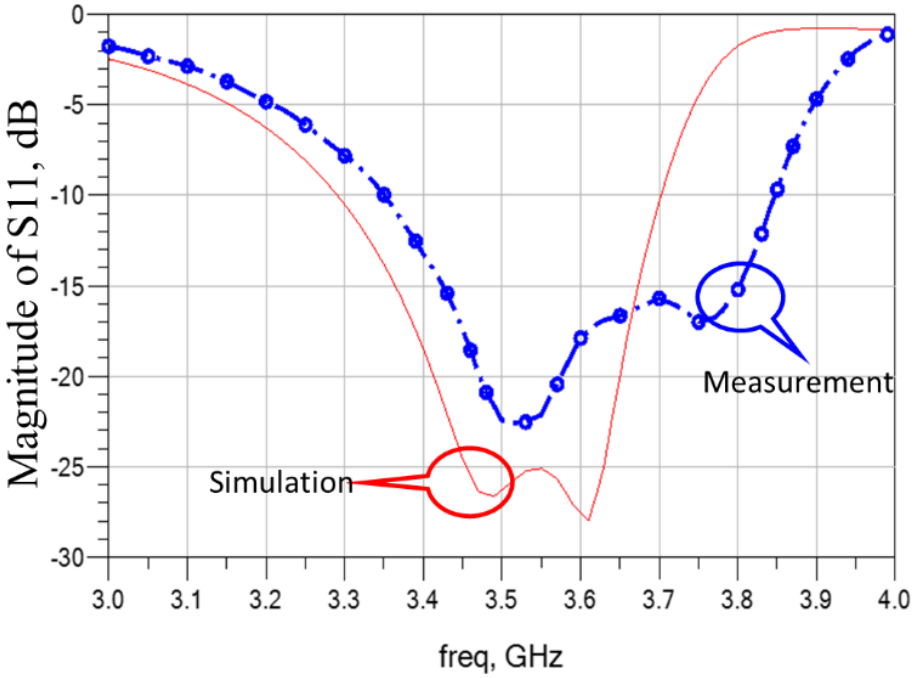

Fig. 3.14 One element antenna measurement and simulation. The blue dotted line is measurement and the red solid line is simulation

Fig. 3.15 Picture of the antenna array and test environment.

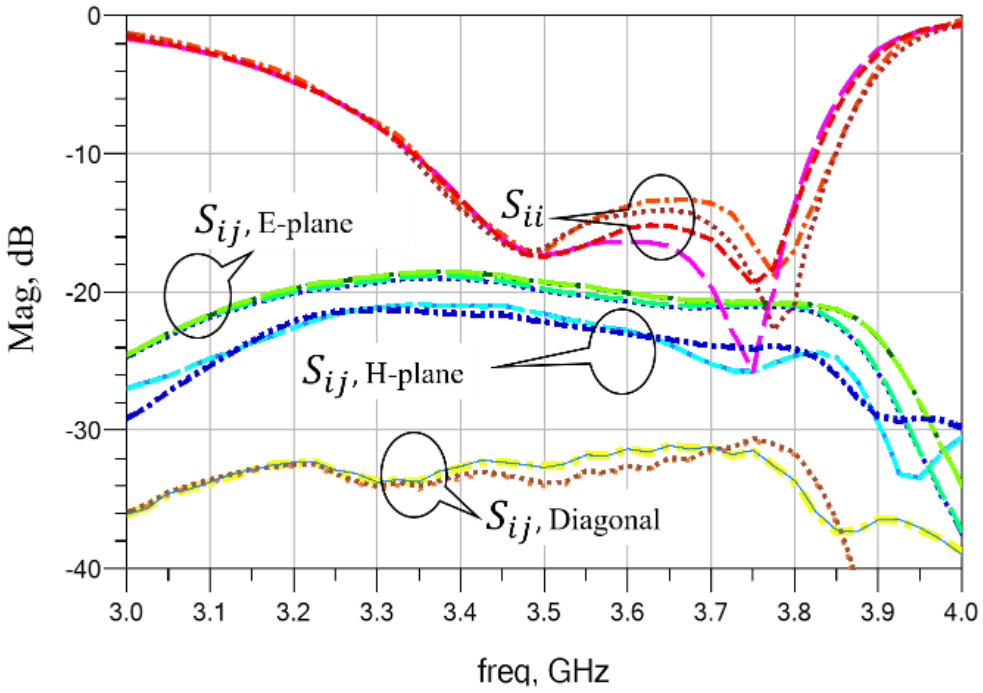

Fig. 3.16 Measured 4-port S-parameters of antenna array

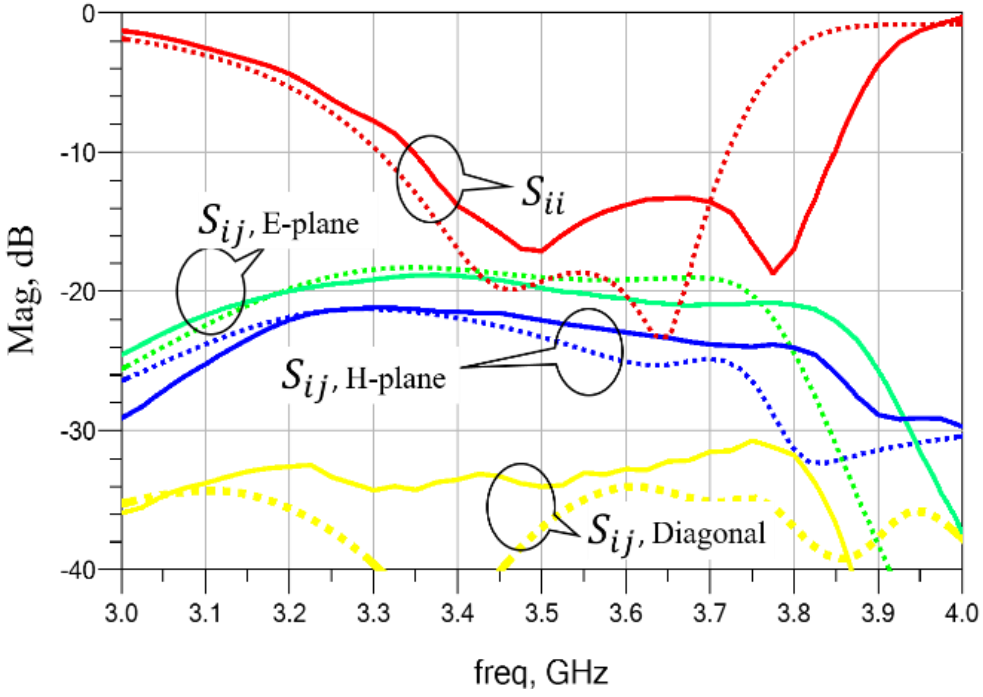

Fig. 3.17 Measurement (solid line) vs. simulation (dot line) for one element of antenna array

3.4 Conclusion

Compared with the antenna used in literatures, e.g. linear dipole array [13], and narrow band low isolation patch array [14], this two-dimension (x and y) antenna array provides a realistic load environment for the PAs in massive MIMO transmitter, enabling the successful investigation on power amplifiers presented in the following chapters.

Chapter 4
Power amplifier array design

4.1 PA fundamentals

4.1.1 Power amplifier basic specifications

Power amplifier converts DC power to AC output, expected to linearly magnify the input small signal into output large signal. It is the most power-hungry component in a transmitter chain, and plays a crucial role in deciding the system power efficiency. The ability of power amplification is defined by the transducer gain *G*.

$$G = \frac{P_1}{P_{avs}} \tag{4.1}$$

where P_1 is the fundamental RF power delivered to the load in Watts and P_{avs} is the power available from the source in Watts. The transducer gain in dB scale is also known as AM-AM. AM-PM is defined as phase variation of the voltage on load as P_1 changes. AM-AM and AM-PM are two indicators of PA linearity performance.

There are two factors describing the conversion efficiency from DC power to RF power, drain efficiency (DE) and power added efficiency (PAE):

$$DE = \frac{P_1}{P_{DC}} = \eta \tag{4.2}$$

where P_{DC} denotes the consumed DC power in Watts. When considering the contribution from gain in the efficiency expression, the power added efficiency is defined as

$$PAE = \frac{P_1 - P_{avs}}{P_{DC}} = \eta * (1 - \frac{1}{G}) \tag{4.3}$$

4.1.2 Operation mode of power amplifier

Currently most base stations employ Field Effect Transistor (FET) to build power amplifier due to its high input resistance and high operation frequency. Ideally a FET can be modeled as a voltage-control-current-source (VCCS) as shown in Fig. 4.1. When neglecting the input, output and package parasitics, I_{ds} vs. V_{gs} and I_{ds} vs. V_{ds} curves as shown in Fig. 4.2 can fully describe the transistor behavior. As V_{gs} increases over V_t (threshold voltage at gate) and before V_{gs_Max}, Ids is controlled by V_{gs} and increased at a slope of g_m. Linear region lies between V_t and V_{gs_Max}. To fully utilize the

power capacity and avoid non-linearity generation, V_{ds} is always set to swing between V_{ds_Max} (decided by transistor breakdown voltage or designed voltage swing) and V_k(knee voltage of the curve I_{ds} vs. V_{ds}), centered at V_{dc}.

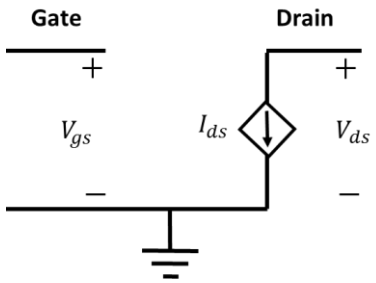

Fig.4.1 Transistor ideal model as VCCS

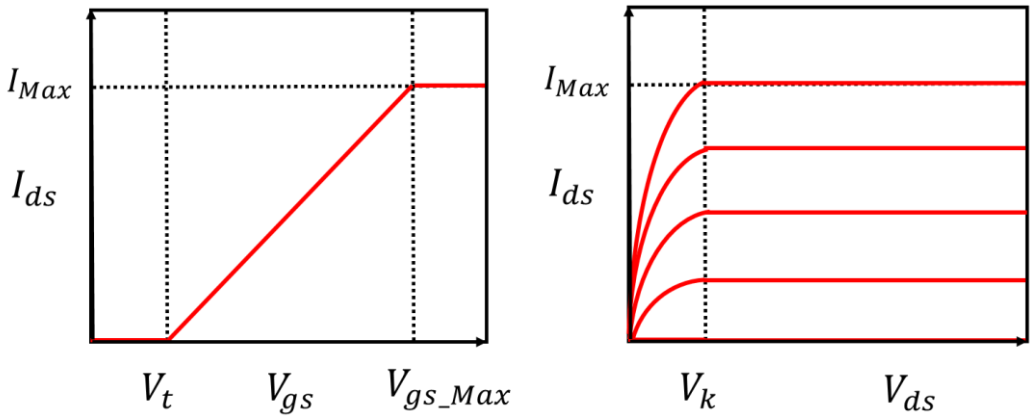

Fig.4.2 DC-IV characterization of transistor

4.1.2.1 Class A PA

Class A is the operation mode when the gate DC bias voltage is set at the middle of V_{gs_Max} and V_t, (V_{gs_Max}+V_t,)/2. The maximum input swing range is between V_t, and V_{gs_Max}. Accordingly, the DC current is half of I_{max} and Maximum AC current amplitude is also half of I_{max}. As explained earlier, the drain voltage swing around V_{dc}, with the largest magnitude of V_{dc} (assume zero V_k). Fig 4.3 shows the load line for Class A operation. Thus the optimal load resistance is

$$R_{opt} = \frac{V_{DC}}{I_{max}/2} = \frac{V_{max}/2}{I_{max}/2} \tag{4.4}$$

The DC power consumption is

$$P_{dc} = \frac{V_{max}}{2} * \frac{I_{max}}{2} \tag{4.5}$$

The peak output power and peak DE are

$$P_{out} = \frac{1}{2}\frac{V_{max}}{2} * \frac{I_{max}}{2} \tag{4.6}$$

$$DE = \frac{P_{out}}{P_{dc}} = 50\% \tag{4.7}$$

Since the transistor turns on for the whole period, the amount of DC consumption is fixed, even though the input power level is zero. This huge wasted power not only lowers efficiency of the transmitter, but also creates heat dissipation burden on cooling systems. Yet its high gain and high linearity performance are demanded in those applications like low noise amplifier (LNA), where linearity is more important than efficiency.

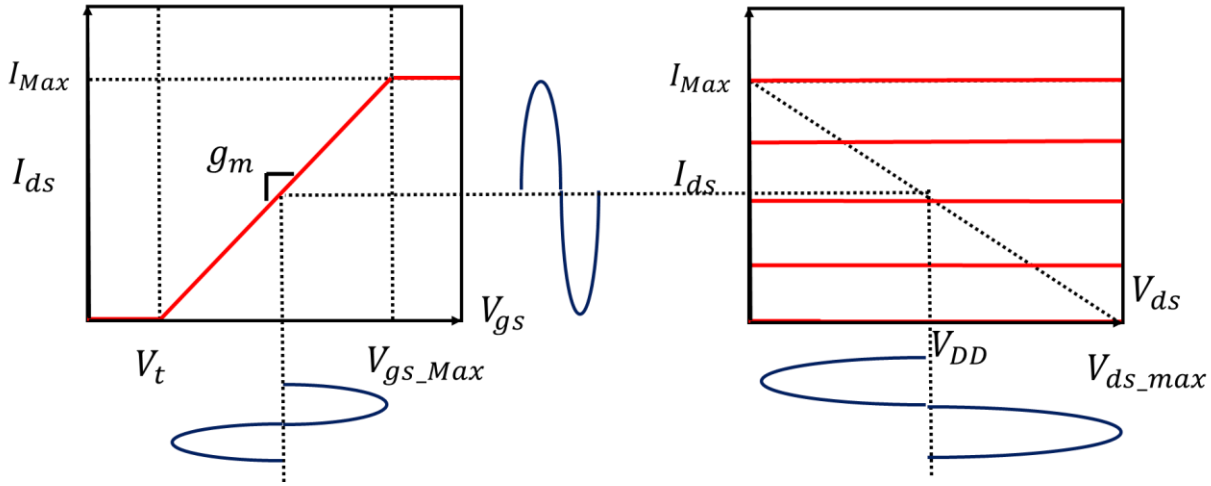

Fig.4.3 Class A operation mode

4.1.2.2 Conduction angle reduced operation mode

The conduction angle is defined as the portion in a whole sinusoidal cycle in which the transistor is conducting current. As shown in Fig. 4.4 (a), conduction angle for Class A is 2π, Class B is π. Any operation between 2π and π is Class AB mode, and those less than π is Class C mode. Reducing conduction angle is realized by lowering down the gate bias voltage, enabling transistor to turn on only after the input voltage exceeds a certain point. Fig 4.4 displays how the input voltage affects the transistor conduction. For a lower bias point, higher instantaneous RF input voltage is needed to turn on the transistor, leading to less conduction time in one signal period.

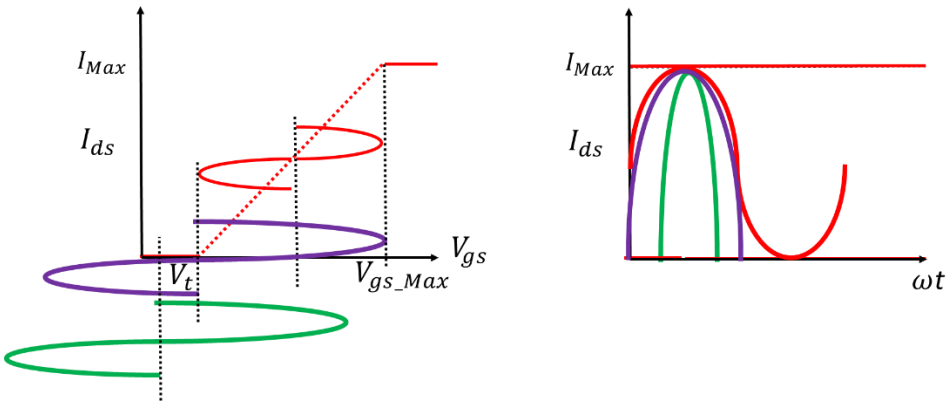

(a) (b)

Fig.4.4 Reduction conduction angle operation mode (a) In DC-IV curve (b) I_{ds} in time domain

As shown in Fig 4.4 (b), when conduction angle is no longer 2 π, drain current will not be a pure co-sinusoidal wave. Fourier series can be used to analyze the fundamental and harmonic composition of the drain current. The current waveform with a maximum drain current I_{max} in Fig 4.4 (b) is

$$I_{ds}(\theta) = \begin{cases} 0, & -\pi \le \theta \le \frac{\alpha}{2} \\ \frac{I_{max}}{1-\cos\left(\frac{\alpha}{2}\right)}\left(\cos\theta - \cos\left(\frac{\alpha}{2}\right)\right) & -\frac{\alpha}{2} \le \theta \le \frac{\alpha}{2} \\ 0, & \frac{\alpha}{2} \le \theta \le \pi \end{cases} \tag{4.8}$$

where α denotes the conduction angle, and θ =ωt. All conduction angle reduced operation modes are assumed that harmonics are shorted and loaded with a pure resistive load. Using Fourier transformation, the DC and fundamental components at peak power are

DC component: $$I_0 = \frac{1}{2\pi}\int_{-\theta}^{\theta} I(cos\omega t - cos\theta)d(\omega t) = I\gamma_0 \tag{4.9}$$

Fundamental component: $$I_1 = \frac{1}{\pi}\int_{-\theta}^{\theta} I(cos\omega t - cos\theta)cos\omega t d(\omega t) = I\gamma_1 \tag{4.10}$$

Current coefficients: $$\gamma_0 = \frac{1}{\pi}(sin\theta - \theta cos\theta),\ \gamma_1 = \frac{1}{\pi}(\theta - sin\theta cos\theta) \tag{4.11}$$

Accordingly, DC power consumption and Pout are

$$P_{DC} = V_{DC} * I_0 \tag{4.12}$$

$$P_{out} = 0.5 * V_1 * I_1 \tag{4.13}$$

To fully utilize the voltage swing at peak power and avoid clipping,

$$V_{1max} = V_{DC} \tag{4.14}$$

$$R_{opt} = V_{DC}/I_1 \tag{4.15}$$

Based on the equations above, it is noticeable that the efficiency changes with conduction angle as well as power level. Lower conduction angles and higher power levels will lead to higher efficiency. Class A mode is only 50% efficient at peak power, and Class C is approaching 100% when the conduction angle decreases toward 0. Class B PA offers 78.5% peak efficiency.

Compared with Class AB and Class C mode, Class A and Class B are more linear because the conduction angle is independent of input voltage, which means that the output current components only change proportionally to input power. However, for other classes of operation, different power level result in different coefficients of the Fourier series for the current in fundamental, hence they are nonlinear by nature. Thus Class B PA is the typical PA type for base station considering the best balance between efficiency and linearity.

4.1.3 Continuous Class-B Operation (Class J operation)

All the operation modes mentioned above assume that purely resistive fundamental termination and open/short circuit for harmonics are needed. This is very difficult for broadband operation since the matching network will show dispersion versus frequency.

Steve C. Cripps in 2009 [35] proposed a set of fundamental/harmonic impedance pairs terminated by which the power amplifier could provide the same output power and efficiency as Class-B operation mode. Instead of assuming all harmonics shorted, the voltage (normalized by the DC component) has the generalized expression of

$$v(\theta) = (1 - cos\theta)(1 - \alpha sin\theta) = 1 - cos\theta - \alpha sin\theta + \frac{\alpha}{2} sin2\theta, \quad -1 \leq \alpha \leq 1 \qquad (4.16)$$

Fourier serises of the half-co-sinusoidal output current:

$$i = I_0 + I_1 cos\omega t + I_2 cos2\omega t + I_3 cos3\omega t + \cdots \qquad (4.17)$$

For the current waveform, we assume it only contains the co-sinusoidal components, which means the current is an even function of conduction angle as shown in fig.4.5. In this case, only the fundamental cosine term in voltage expression is dissipative. The fundamental sine term introduces the imaginary part for fundamental impedance. Second harmonic impedance only has imaginary part, determined by the sine term of second harmonic in voltage expression. Alpha defines the design freedom of Class J power amplifier.

When alpha is zero, equation (4.16) is reduced to the form of conventional class-B mode. The difference appears when α is not zero, and in that case, fundamental impedances all have the same real

part equal to the optimum resistive load for class-B and various imaginary part. Based on the current and voltage waveform, the imaginary part of fundamental and second harmonic are calculated by

$$\frac{-V_{DC}}{I_1} < X_1 < \frac{V_{DC}}{I_1} \tag{4.18}$$

$$\frac{-V_{DC}}{2I_2} < X_2 < \frac{V_{DC}}{2I_2} \tag{4.19}$$

I1 is shown in 4.1.1, and I2=

$$I_2 = \frac{1}{\pi}\int_{-\theta}^{\theta} I(cos\omega t - cos\theta)cos2\omega t\, d(\omega t) = 2sin\theta - \frac{4}{3}\, sin\theta^3\text{-}cos\theta sin2\theta \tag{4.20}$$

$$I_2 = \frac{2I}{3\pi} \quad \text{when } \theta = \frac{\pi}{2}$$

Thus, the termination condition is summarized as

$$Z_{f0} = {R_{opt}}^B + j^* \alpha * {R_{opt}}^B\ ,\ {R_{opt}}^B \text{ is the optimum impedance of Class-B mode} \tag{4.21}$$

$$Z_{2f0} = -j^* \alpha * \frac{3\pi}{8}{R_{opt}}^B, -1 \le \alpha \le 1 \tag{4.22}$$

With the same DC and fundamental dissipative component, the Class-J operation mode could have theoretically the same output power and drain efficiency (78.5%). The appearance of the imaginary part at fundamental frequency enlarges the voltage swing, which could cause the transistor clipping. However, the out-of-phase non-zero termination for 2nd harmonics is introduced to bring the lowest value back to above zero so that the allowed voltage swing is fully utilized, meanwhile, linearity is guaranteed by avoiding clipping. Fig.4.5 shows the fundamental and 2nd harmonic impedances of Class-J operation on the Smith Chart with reference impedance of ${R_{opt}}^B$.

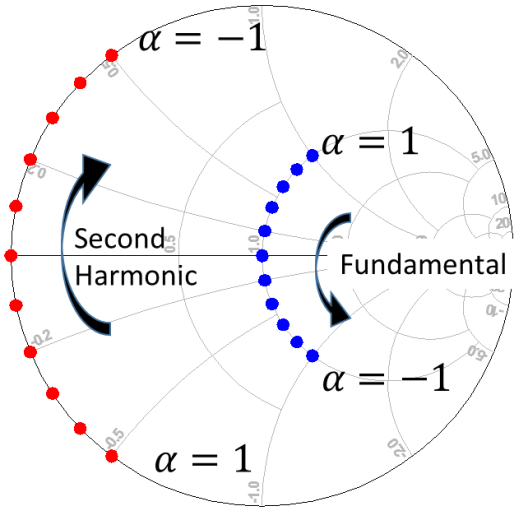

Fig.4.5 Class J design space illustrated in Smith Chart including fundamental impedance (blue) and second harmonic (red).

4.2 Single way PA design

In order to support wideband signals transmission, the designed PA should be able to provide optimum efficiency in broadband operation. As shown in section 4.1.3, Class J design space is a powerful method to realize it. The following contents introduce the design methodology for matching network aiming at taking advantage of Class J design space, the stabilization block, and EM simulation results of the designed broadband high efficiency PA.

4.2.1 Output matching

A well-designed wideband patch antenna has the load impedance as shown in Fig 4.7. The antenna is matched for 50 Ohm. The fundamental impedance spreads along the curve 50+Xj on the Smith Chart, with high frequency band showing the inductive characteristic and low frequency band showing the capacitive characteristic. The second harmonics have the similar distribution pattern. However, the Class J power amplifier requires the inverse properties of the load pairs where capacitive fundamental loads have an inductive second harmonic loads and inductive fundamental loads have a capacitive second harmonic load. This load requirement can be realized by adding a 90 degree electrical length transmission line which makes the fundamental impedance turn 180 degree and second harmonic turn 360 degree around the Smith Chart center.

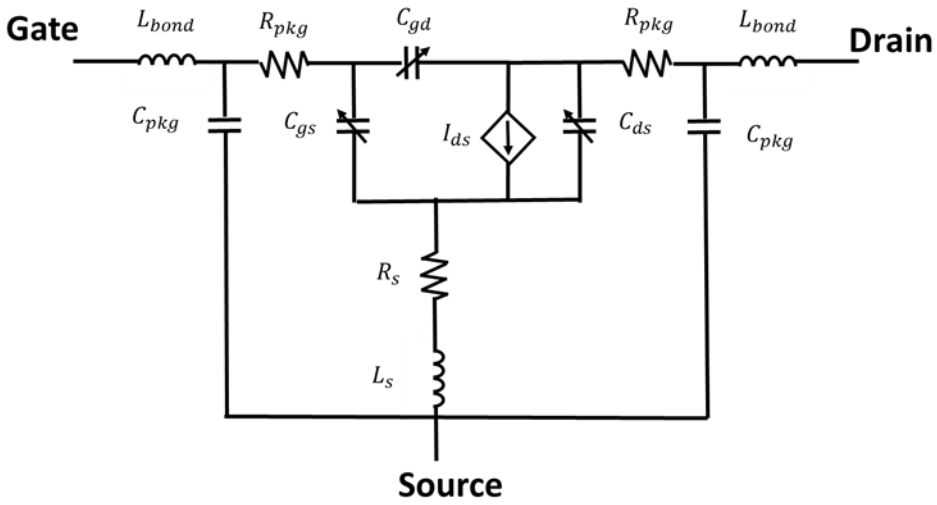

Fig.4.6 Compact small signal model of packaged transistor

The commercial transistors used in power amplifiers contain intrinsic and extrinsic parasitics, posing major challenges when designing matching networks. The parasitics as shown in Fig. 4.6 are in-

troduced by the overlapped electrode interface (C_{ds}, C_{dg} andC_{gs}), bond wire (L_{bond},) or package (C_{pkg}) and pad (C_{pad}). Parasitics caused by passive component are mostly linear, and those introduced by active part will show nonlinearity to some degree. For Laterally Diffused MOSFET (LDMOS), the output capacitance C_{ds} is strongly nonlinear. For gallium nitride (GaN) high-electron-mobility-transistors (HEMTs), C_{ds} is slightly nonlinear. At the target frequency, transistor parasitics have non-negligible effects, thus the output matching network should take the parasitics of transistor into account.

In this design, the packaged GaN HEMTs CGHV1F006S from Cree is used. Cold-FET technology was used to extract the compact model and get access to the intrinsic current generator plane after de-embedding the parasitics. The optimum load for this transistor to operate in Class B mode with 28V Drain voltage is around 60 Ohm according to the DC-IV curve. The output matching network composed of transmission lines and stubs along with the parasitics are put together to run the optimization. In the end, the output matching network together with the parasitics transfer the antenna load in Fig.4.7 into the desired intrinsic load in Fig. 4.8. As is explained in the previous section, the extended design space provides more flexibility in impedance matching and thus a path toward broadband operation.

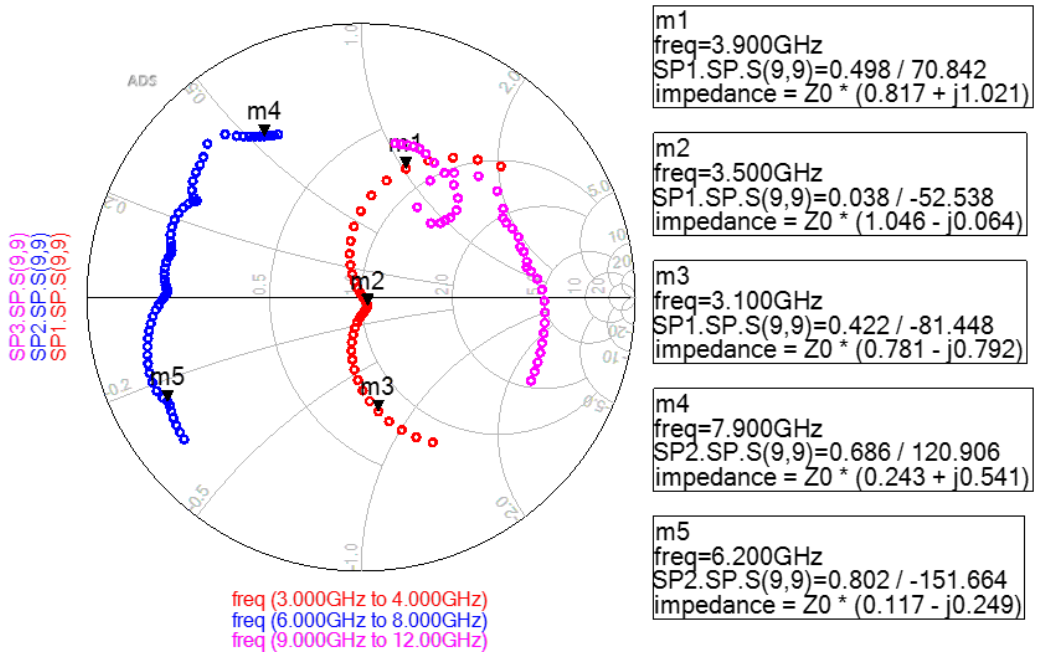

Fig. 4.7 Antenna impedance plot at fundamental, second, and third harmonic frequency, used for PA output matching design

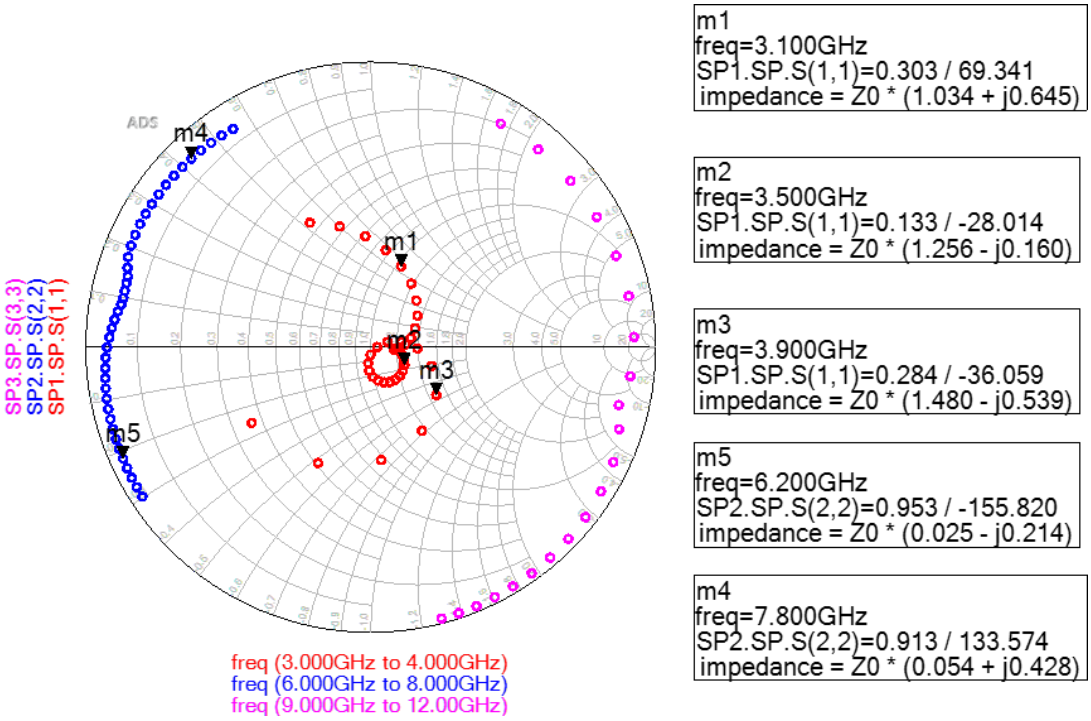

Fig. 4.8 Intrinsic Drain impedance plot at fundamental, second, and third harmonic frequency

4.2.2 Input matching and stability

Input matching network is a critical part of the power amplifier. It determines the overall gain, linearity and stability. At the input, a major design challenge is that the input capacitor C_{gs} is strongly nonlinear. The allowed gate voltage range of the transistor is from -10 to 2V. In this range, C_{gs} varies from the lowest value below 2 pF to highest value of 3.4 pF. The nonlinearity of the input capacitance makes it tedious to carry out any analytical investigation of input matching. So the source-pull technique is used to find the optimum source impedance.

The stability circuit is two resistors connected to the gate RF path and gate bias path, aiming at stabilizing RF and Baseband respectively. A large capacitor is connected in parallel with RF path resistor to short the resistor in RF frequency so that the gain in RF frequency range will not be influenced. The input matching network is optimized with a capacitor as DC block and short stub as gate biasing path.

4.2.3 EM simulation and layout

The matching network is initially designed in schematic and then the corresponding layout is generated. Space-mapping technique is employed to reduce the discrepancy between schematic and EM simulation due to the inaccuracy of schematic in modelling layout coupling.

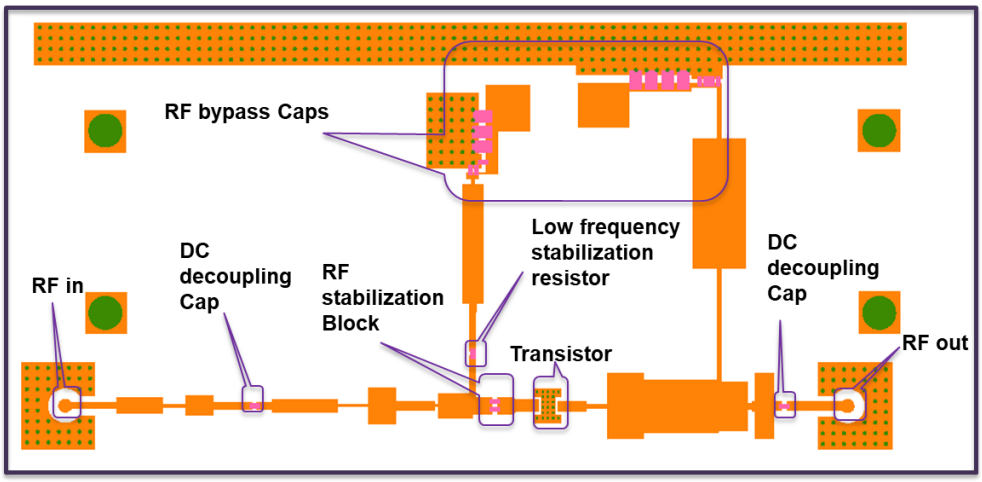

Fig. 4.9 Single way PA layout with lumped elements denoted

The PA is etched on a 4.5 inch × 2.25 inch × 16 mil RO4003C substrate, with dielectric constant 3.55. Fig 4.9 is the final layout of single-way PA, where all the lumped elements are denoted. All the transmission lines are simulated in both HFSS and ADS momentum to ensure simulation accuracy.

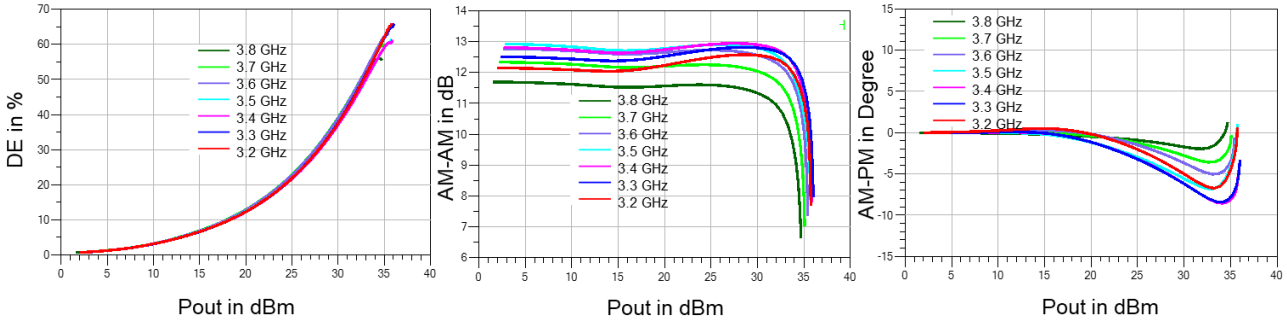

Fig. 4.10 CW simulation results for 50 Ohm loaded case (a) Drain efficiency (b) AM-AM (c) AM-PM

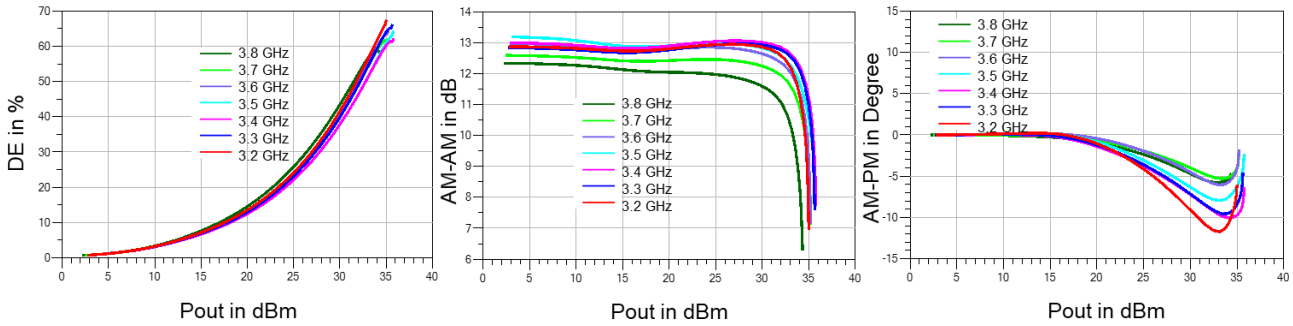

Fig. 4.11 CW simulation results for Antenna loaded case (a) Drain efficiency (b) AM-AM (c) AM-PM

The PA CW simulation results with 50 Ohm load and antenna load are given in fig 4.10 and fig 4.11, respectively. Input power is swept from -10 dBm to 28 dBm, and the frequency range from 3.2 GHz to 3.8 GHz is evaluated. Since the PA is designed based on antenna load for high efficiency operation from 3.2 GHz to 3.8 GHz, better performance is achieved with antenna load than with 50 Ohm load at edge frequencies. This is because that the matching network is designed for transferring the antenna impedance, which has large imaginary part at edge frequencies, to Class J impedance space. With antenna load, Peak Drain efficiency is all above 59% from 3.2 GHz to 3.8 GHz, however with 50 Ohm load, at 3.8 GHz peak DE drops to 54%. Gain variations at each frequency before Pout 6 dB back-off are within 0.3 dB for antenna load, and within 0.5 dB for 50Ohm load. The simulated P_{sat} is from 34 to 36.5 dBm over the frequency range. The AM-PM curves are indicator for output phase variation. For beamforming system, how well the phases are combined decides the direction and quality of signal. From the Fig.4.10.and Fig.4.11, the phase variation are within 8 degrees and 12 degrees respectively.

The connector between PA and antenna can be eliminated in a multi-layer PCB stack-up as shown in Fig 4.12 by a through via connecting the PA output and antenna feeding line.

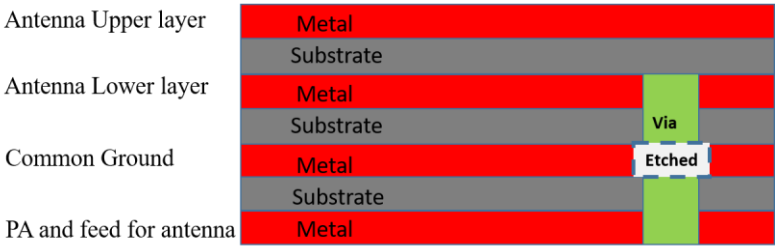

Fig. 4.12 A possible integration stack-up for PA and Antenna

4.3 PA array design

4.3.1 Four-channel PA layout

In order to make the PA-Antenna co-design feasible and preserve the scalability to larger array, alignment and miniaturization are necessary so that antenna and PA can be directly connected together. Fig.4.13 depicts the bended two by two PA array, which keeps the same performance as the single way design. The whole circuit is symmetric about the center. Four inputs and two DC bias pads are at the edge of board for easy access to connectors and wires. Four RF output positions are aligned with the antenna array designed in the last chapter. Grounded via fence are added around each PA to reduce the mutual coupling.

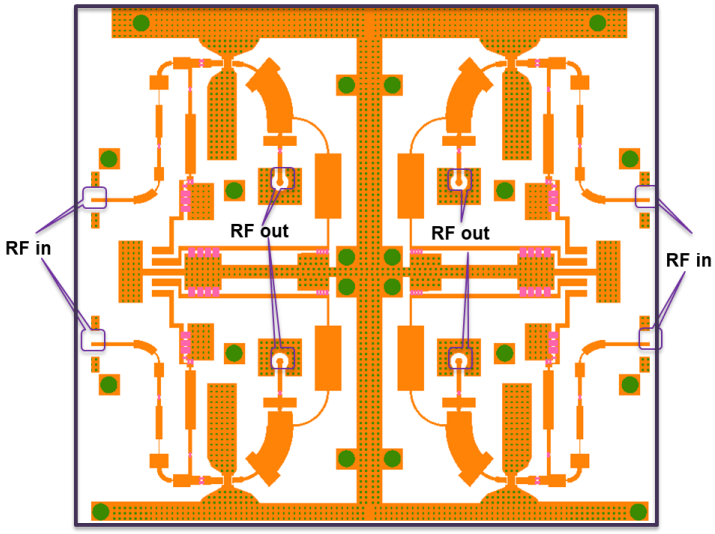

Fig. 4.13 PA array layout

4.3.2 Four-channel PA-Antenna simulation

In chapter 3.2, the active impedance variation of the two by two antenna array has been displayed under the different phases and magnitudes circumstances. When the antenna and PA array are connected, they form a front-end that can be used to study the effect of active impedance variation on PA performance. In ADS, the four PAs' outputs are connected to each port of the antenna array, which is a S4P file generated from HFSS. Since input power level itself has significant impact on DE, for a better comparison of DE variation, only different input phases of PA while keeping the input magnitude the same, are simulated in this case, which corresponds to RF beamforming scenario. Two antenna arrays with high (-19 dB) and low (-28 dB) mutual coupling level respectively, connected with

the same PA array are studied. As shown in Fig.4.14, where the four PA performance are displayed with different colored lines when steered for 30 degree at 3.5 GHz, only two different behaviors are observed in impedance variation as expected because of the symmetric input signal combination of 2×2 array. Around 3% DE variation, 1.2 dB gain variation, 2dB output power variation, and 2 degree AM-PM variation are observed from high coupling level case. On the contrary, only 1% DE variation, 0.3 dB gain variation, 1dB output power variation, and 1.5 degree AM-PM variation are observed in the low coupling level case.

With selected phase combination for four inputs, around 3% DE variation, 0.8 dB gain variation, 2 dB output power variation, and 5 degree AM-PM variation are observed from high coupling level case. On the contrary, only 1% DE variation, 0.5 dB gain variation, 1dB output power variation, and 2 degree AM-PM variation are observed from low coupling level case as shown in Fig.4.15.

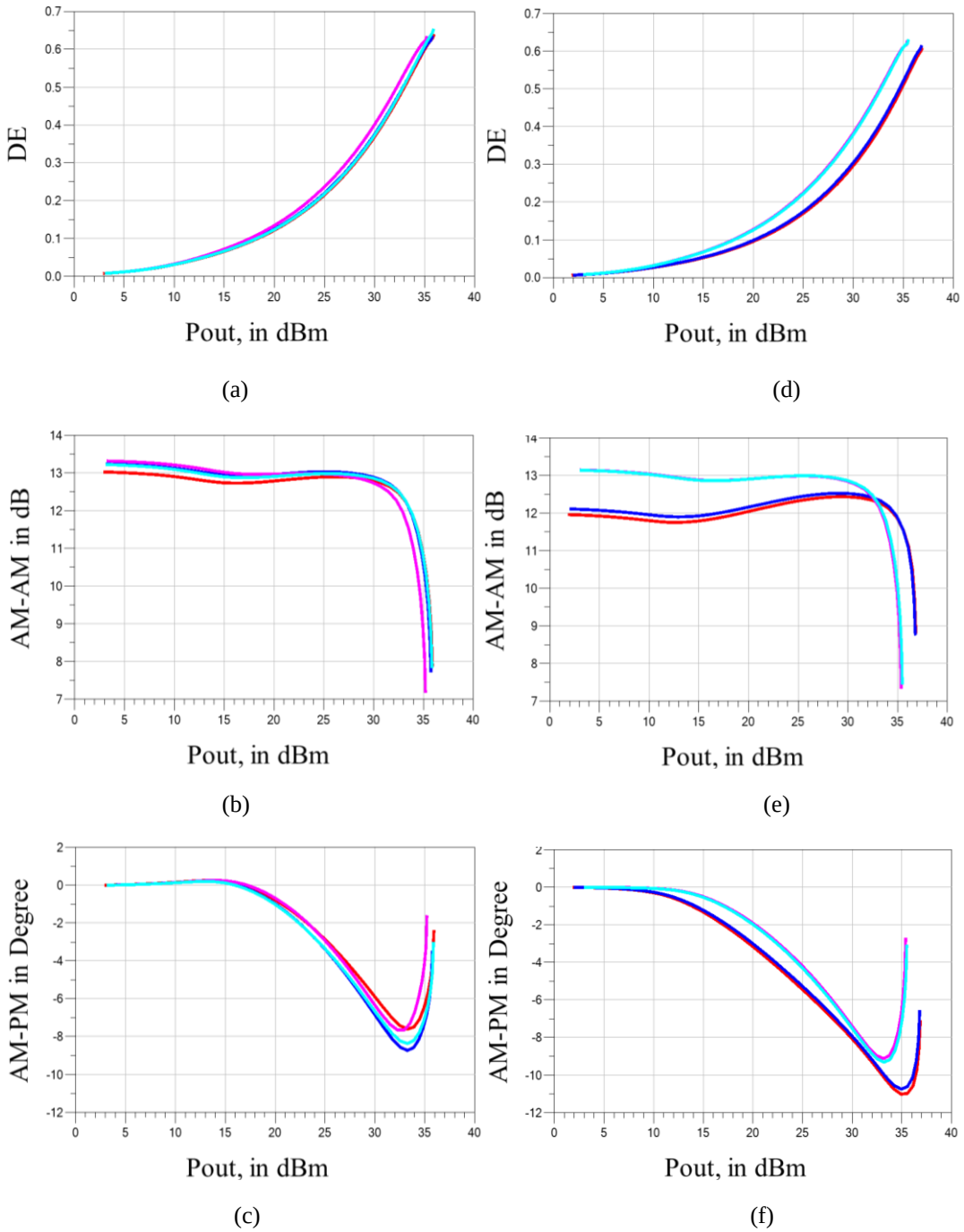

Fig. 4.14 Four PA CW performance variations when array is steered for 30 degree at 3.5 GHz. (a),(b),(c) corresponding to -28 dB isolation array and (d),(e),(f) corresponding to -19 dB isolation array.

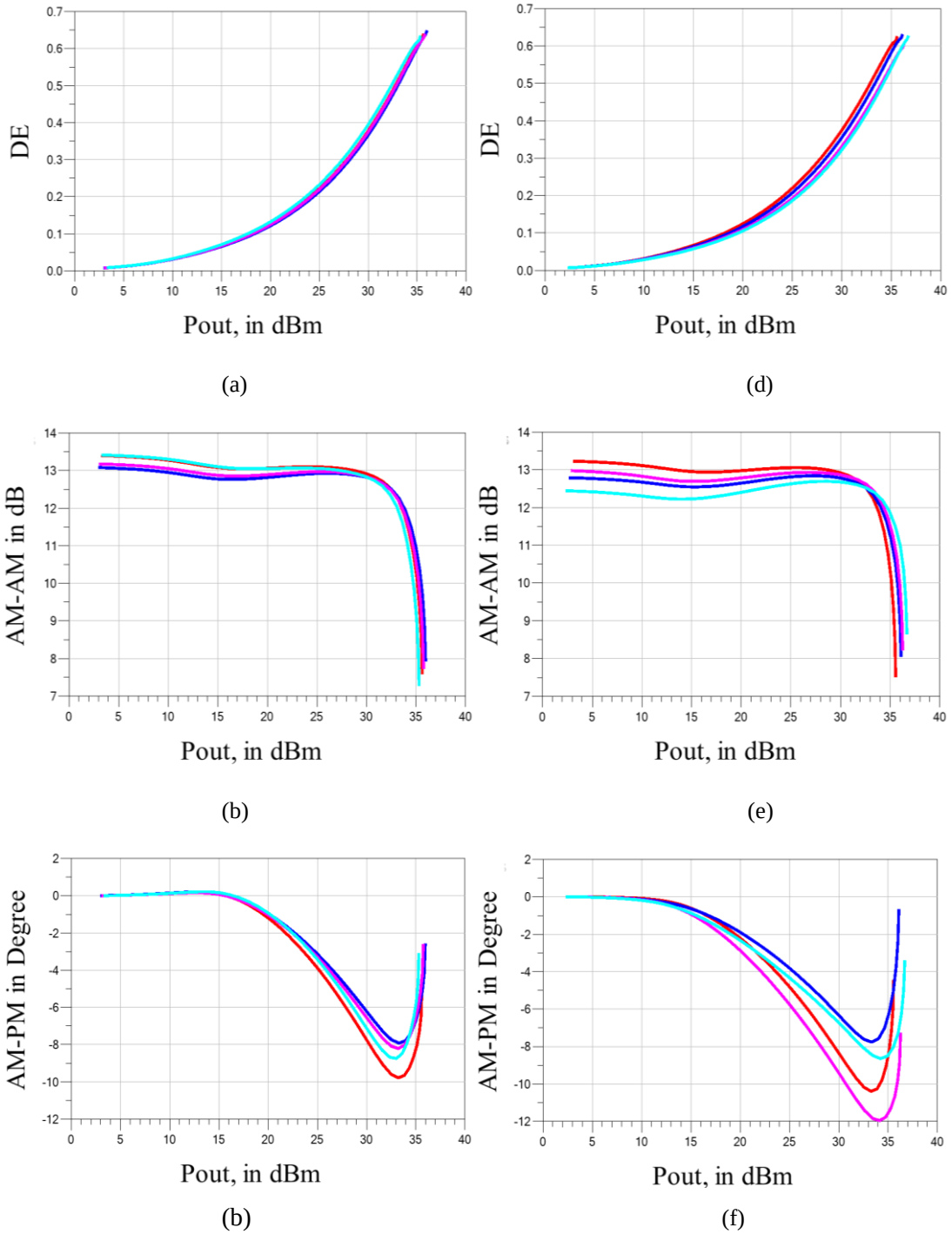

Fig. 4.15 Four PA CW performance variations when having randomly selected phases at 3.5 GHz (a),(b),(c) corresponding to -28 dB isolation array and (d),(e),(f) corresponding to -19 dB isolation array.

4.4 PA Measurement

4.4.1 Continuous Wave (CW) measurement

The PA board is fabricated on RO4003C substrate as shown in fig.4.16 (a). To provide enough driving power to the PA input when performing large signal test, four NXP MMZ38333BT1 amplifiers and one ZHL-42 amplifier are used as drivers. CW measurement setup is shown in Fig. 4.16 (b). A 30 dB attenuator is added after the PA to protect the nonlinear network analyzer Keysight PNA-X N5247A. Calibration is performed by Ecal module and power meter at the driver output plane and PA output plane.

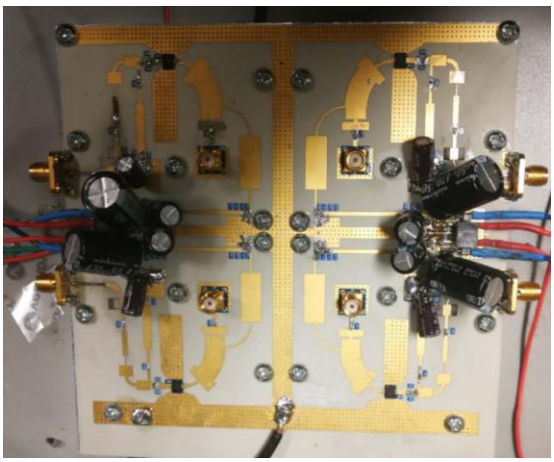

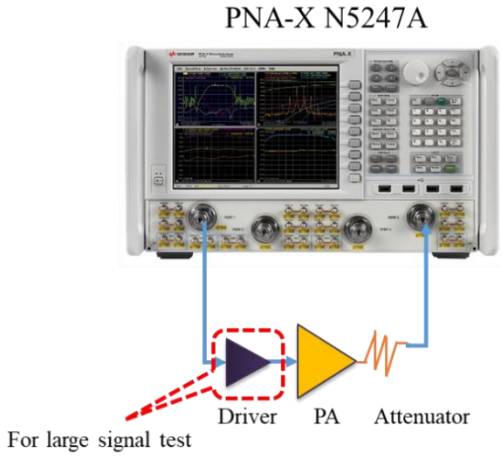

(a) (b)

Fig. 4.16 (a) PA board (b) CW measurement setup

Firstly, the small signal performance is characterized. Input matching (S_{11}), output matching (S_{22}) and gain (S_{21}) are plotted in fig 4.17 for all the four PAs. Due to the assembling error, the four PA have observable different response.

Then the large signal CW measurement is performed based on 50 Ohm load with ZHL-42 amplifier as driver for the single way PA and the measurement results are shown in Fig.4.18. By employing class J design space, the designed PA achieves high efficiency matching from 3.2 to 3.8 GHz. The peak drain efficiencies are all above 60 % except for 3.2 GHz. The low efficiency at 3.2 GHz is caused by the higher output potential. The AM-AM curve at 3.2GHz shows that at the largest driving point, the PA is only compressed by less than 1dB, and output power is around 35 dBm. It is a fairly reasonable speculation that with higher input drive at 3.2 GHz, the PA can provide higher output power and drain efficiency. We can see that compared with the simulation in Fig.4.10, measurement

shows is quite close to the measurement around the center frequencies 3.4, 3.5 and 3.6 GHz. However, at edge frequencies, there is a certain difference. The discrepancy can be attributed to the inaccuracy of large signal model of the transistor and the dielectric constant of substrate.

In addition, large signal CW measurement for PA array is also conducted with the four NXP MMZ38333BT1 drivers as shown in Fig.4.19. Since the NXP drivers are designed for 3.4GHz to 3.6GHz, the overall performance is constrained within this range. From 3.2GHz to 3.8GHz, the driver has 5 dB variation in AM-AM and ± 2 degrees variation in AM-PM, which all contribute to the performance degradation of the transmitter. However, the NXP amplifier offers the ability to be integrated with the PA array compactly and the capacity to be scaled to a larger array, and it also costs lower than ZHL driver.

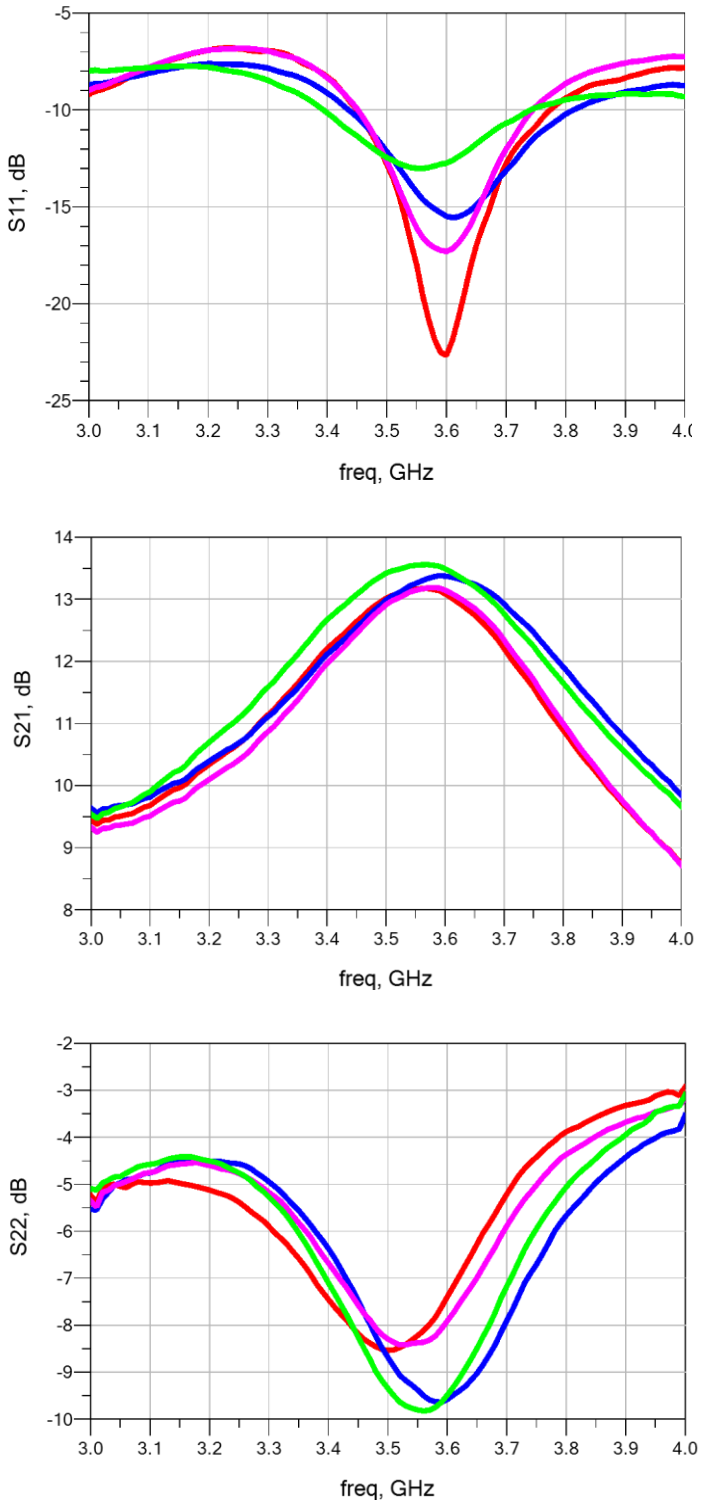

Fig. 4.17 Small signal performance for the PA array; each color represents one PA

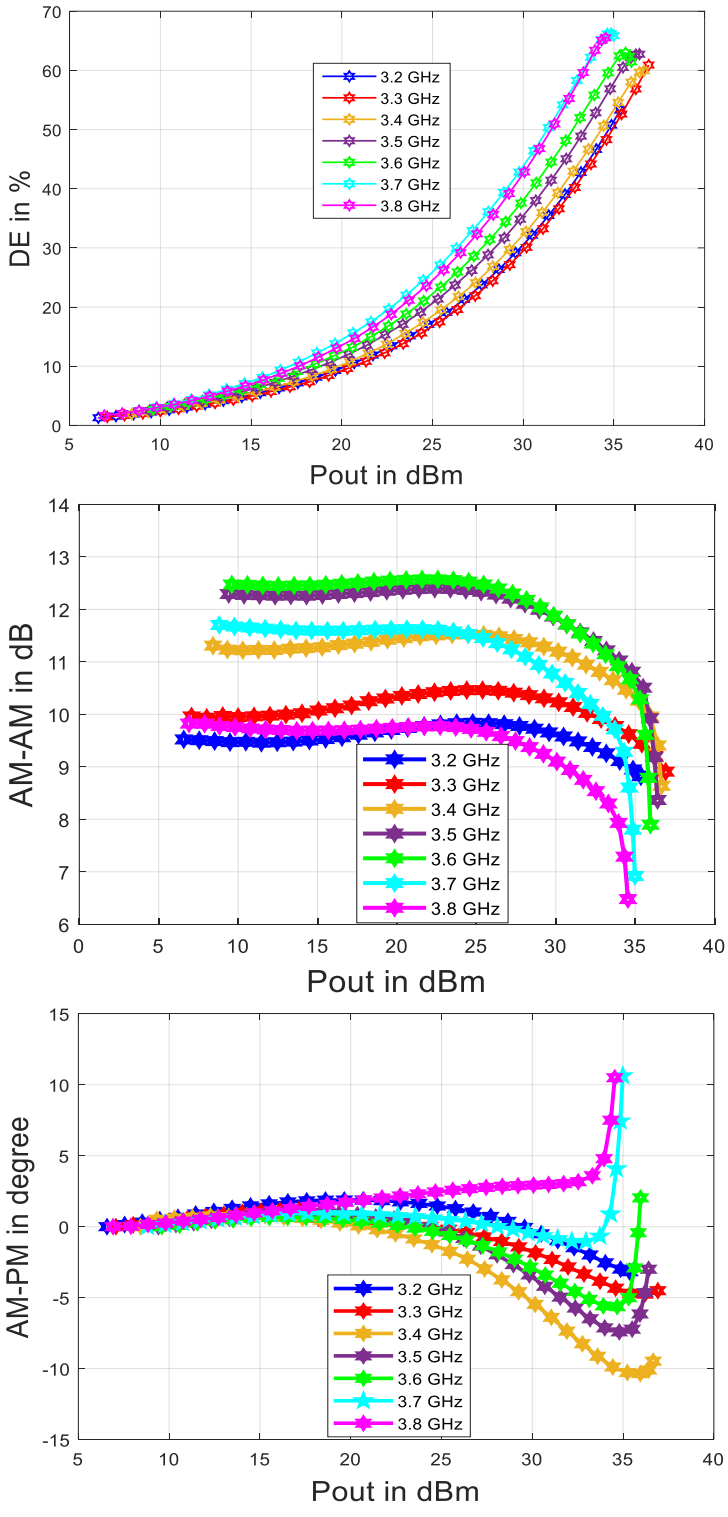

Fig. 4.18 Measured large signal CW performance for single way PA with 50 Ohm load

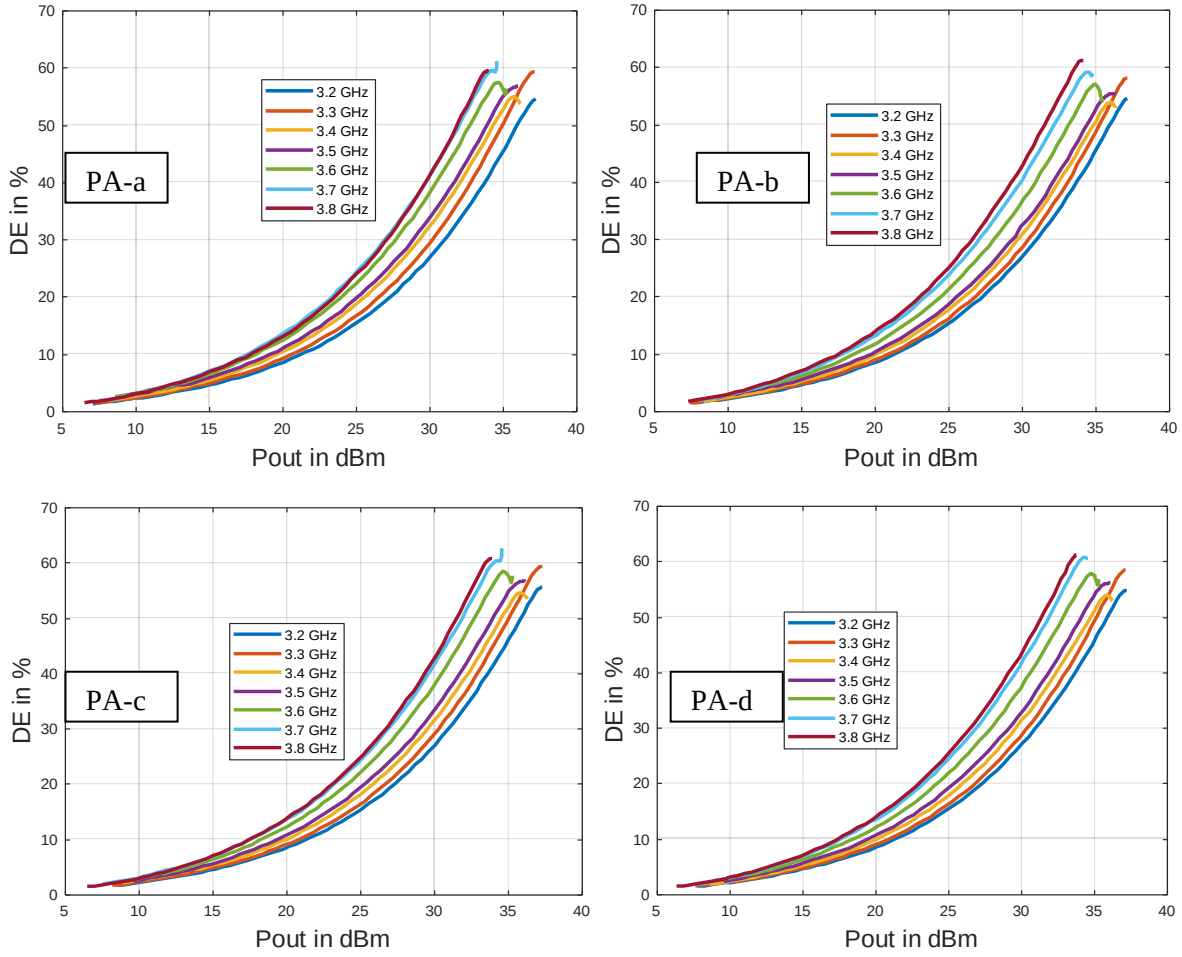

(a) DE of four PA elements

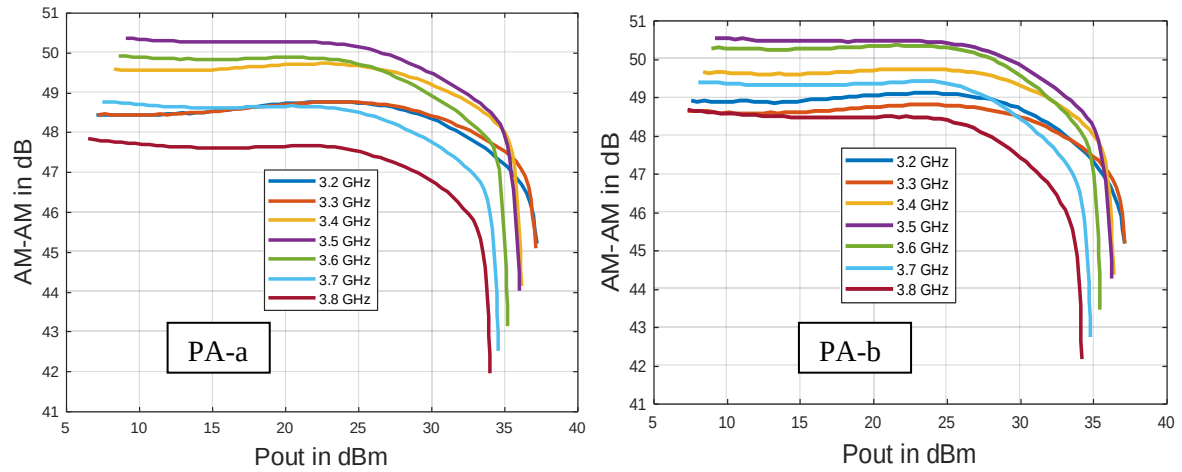

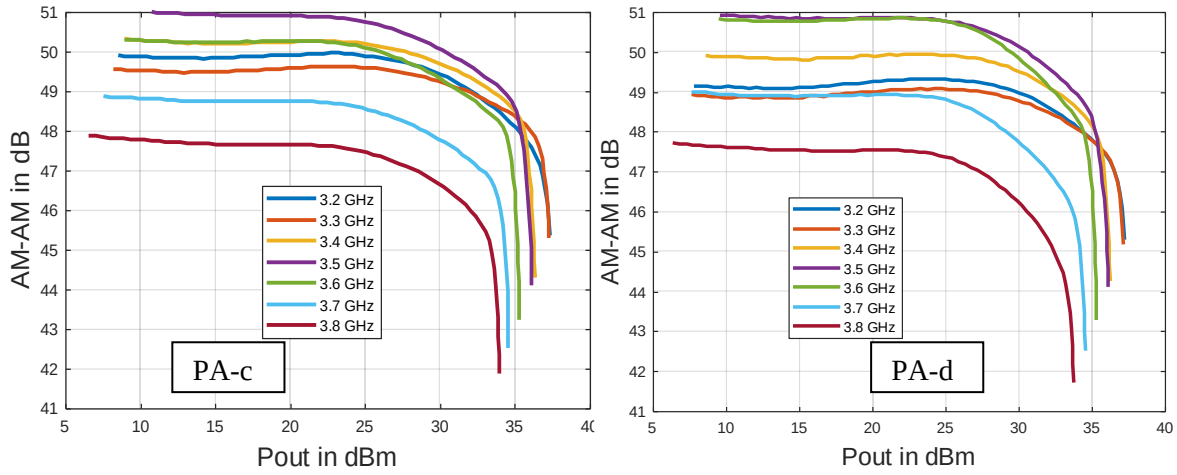

(b) AM-AM of four PA elements

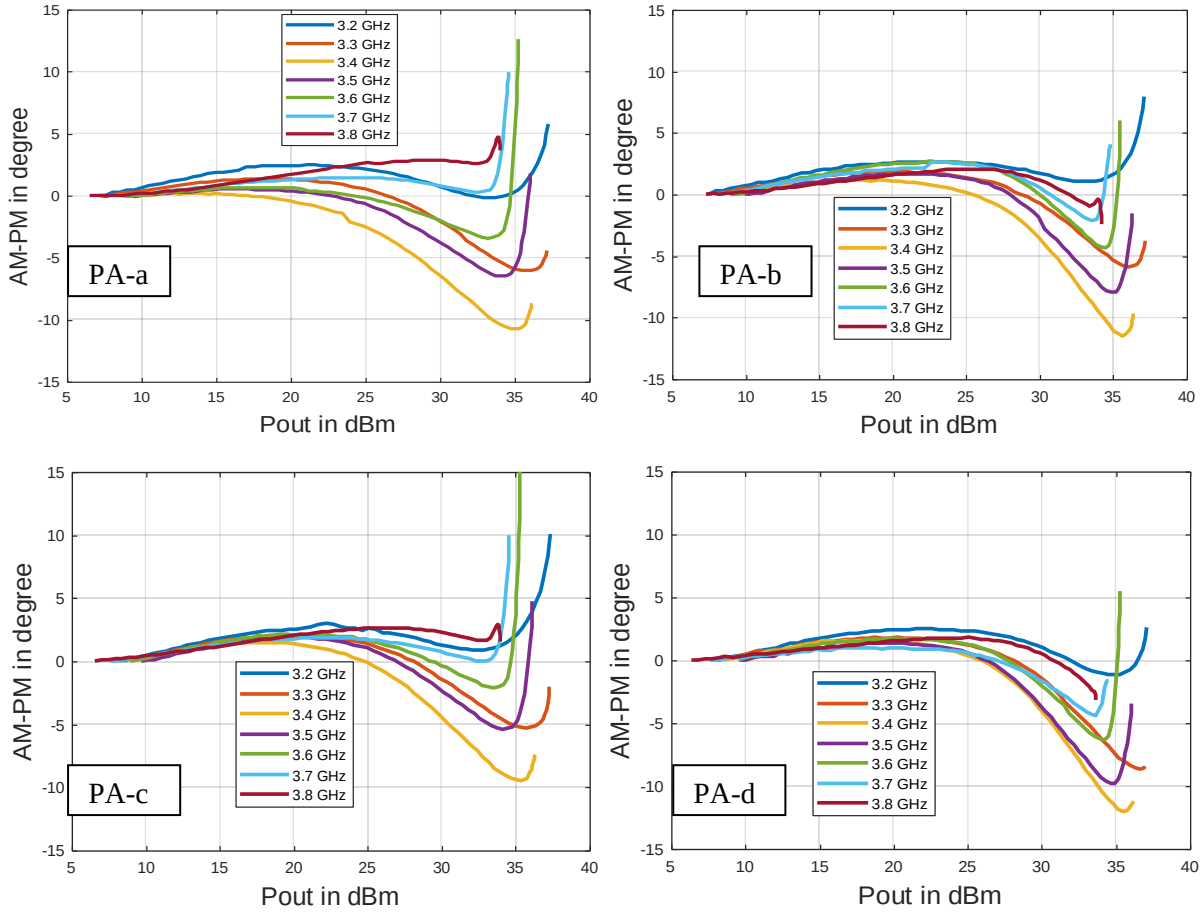

(c) AM-PM of four PA elements

Fig. 4.19 Measured large signal CW performance for PA array with 50 Ohm load

4.4.2 Modulated signal measurement

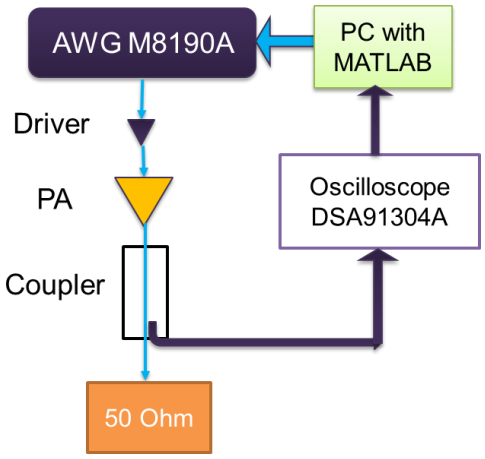

Fig. 4.20 Modulated signal measurement setup for one PA

For modulated signal test, a two channel arbitrary wave generator (AWG) generates OFDM signals with different configurations, amplified by NXP drivers and PAs. In order to capture the output signals of the PA, a directional coupler is inserted between PAs and loads. Then the coupled outputs is captured by the oscilloscope DSA91304A. A PC with MATLAB controls input signal, processes the received signal from oscilloscope and performs DPD for whole chain. Fig.4.20 depicts the modulated signal measurement setup. The DPD engine is 72-coefficient CRV Pruned for all the DPD measurement in this work. The signal peak to average ratio (PAPR) is 8 dB, and average DE is around 23%.

As a first step to assess the performance of the designed PA array under modulated signal, the results obtained using a one PA with 50 Ohm load, driven by various configurations of modulated signal at 3.5GHz (continuous 100, 200 MHz and carrier aggregated “101”, “1001” with 50 MHz signals) are shown in Fig.4.21 and table 4.1. It can be seen that the designed PA demonstrates the excellent linearizability even with such wideband signals.

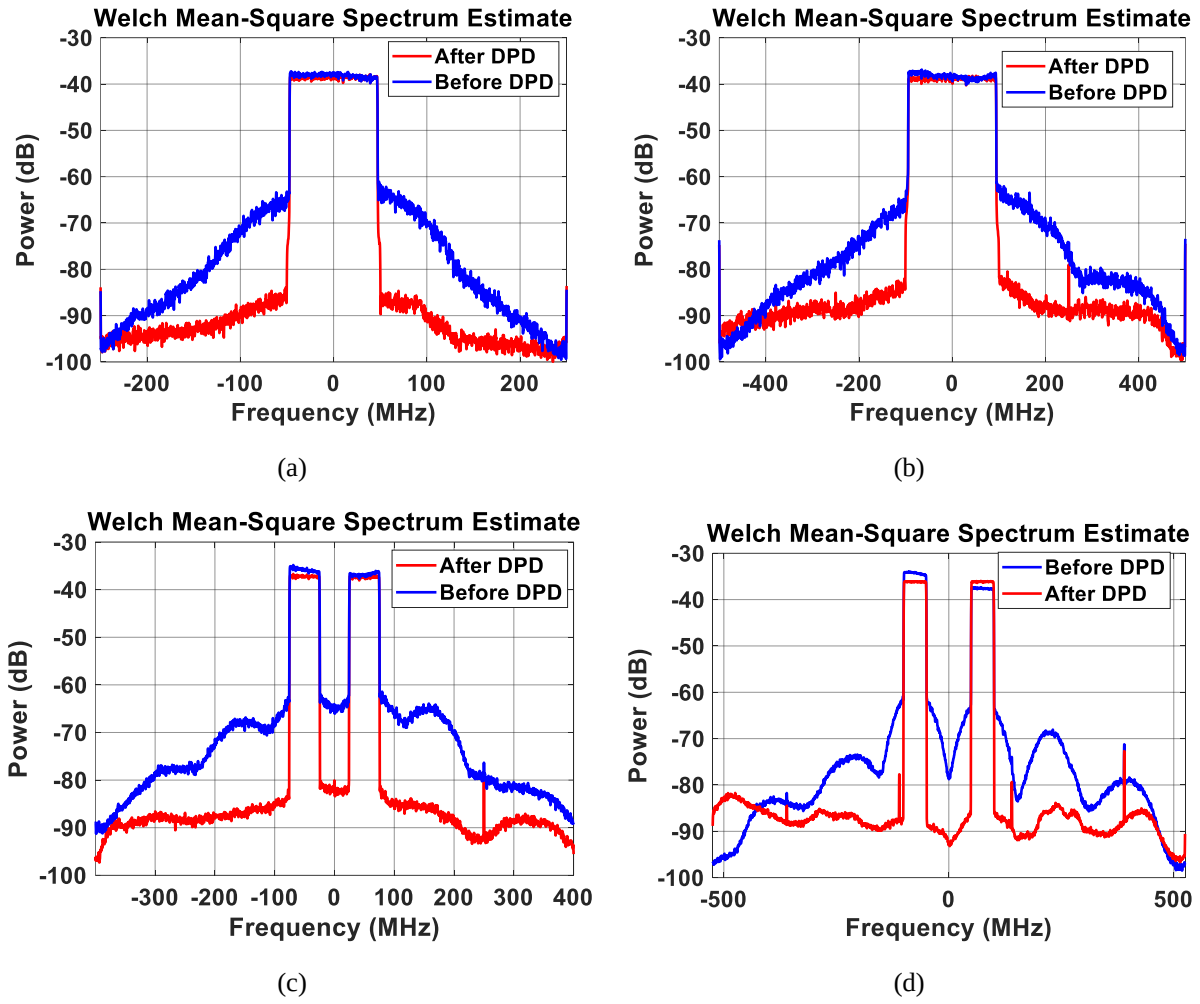

Fig. 4.21 Modulated signal measurement with 50 Ohm load (a) Continuous 100MHz (b) Continuous 200MHz (c) 150 MHz carrier aggregated signal by 50MHz "101" (d) 200 MHz carrier aggregated signal by 50MHz "1001"

	ACPR(L/U) Before DPD (dB)	RNMSE Before DPD (%)	ACPR(L/U) After DPD (dB)	RNMSE After DPD (%)
100 MHz	30.9 / 29.2	8.9	50.1 / 50.3	0.7
200MHz	32.8 / 30.0	9.8	47.5 / 47.4	1.1
"101"with 50MHz	33.4 / 30.1	9.1	49.9 / 51.9	0.7
"1001"with 50MHz	34.0 / 30.5	9.8	46.2 / 47.3	1.3

Table 4.1 Single PA modulated signal measurement with 50 Ohm load

4.5 Conclusion

Chapter 4 introduces the details of PA array design and measurement. The high efficiency PA array has excellent wideband linearizability (with 200MHz modulation bandwidth signal at 3.5GHz). Together with the designed antenna array, the following system investigation is able to be performed. In the next chapter, we will assess the linearizability of PA in array configuration.

Chapter 5
System measurement and analysis

When the antenna and PA arrays are connected, they form a RF front-end that is used to study the effects of the antenna load modulation using realistic modulated signals for 5G system. In the following section, different configurations specifically devised to investigate the effects of coupling due to the PA board and finite isolation between the antenna elements, as well as the extent of the nonlinearity of the PA elements.

5.1 PA board coupling effect investigation

First, the coupling effect of the PA board is studied. The PA array is composed of four closely arranged units. Although ground via fence is added between each other to reduce the coupling caused by shared substrate, the radiation from matching network is not a negligible source that introduces coupling over the air. In the measurement setup shown in fig.5.1, two two-channel AWGs are used to provide four independent OFDM signals, the signals get amplified by divers and PAs. The couplers are added between each PA and 50 Ohm load to capture the PA output signals, which are then sent back to a spectrum analyzer UXA N9040B or oscilloscope DSA91304A to perform DPD. During the test, the average output power of each PA are kept the same and only one PA is linearized by SISO DPD, which is equivalent to using four separate SISO DPD trainings to linearize the four paths when studying the SISO DPD linearizability for the PA experiencing load variation. But linearizing four paths simultaneously needs four sets of receiving instruments and complicated aligning, hence linearizing one channel is cost-effective in this study. Two cases are compared here: when one channel is transmitting and when four channels are transmitting. Since the PAs have the same 50 Ohm load, any difference between the four transmitting case and one transmitting case should be attributed to the PA board coupling. 100MHz and 20MHz modulation bandwidth signals both are used for this study.

Summarized in table 5.1, with 20MHz modulation bandwidth signal, ACPR degradation due to coupling effect before DPD is 2 dB, and after DPD is 3 dB. NMSE can also experiences this degradation. With 100MHz bandwidth signal, because the PA nonlinearity dominates the ACPR results, the ACPR degradation is barely distinguishable, but the increased NMSE shows the same trend as in 20 MHz case. By comparing the ACPR after DPD, we know that the PA board does introduce minor coupling and the effect cannot be compensated by SISO DPD. The coupling impact only becomes

more distinguishable when the ACPR is below 50 dB, which gives us the confidence that the coupling effect caused by substrate will not mask the distortion of antenna coupling.

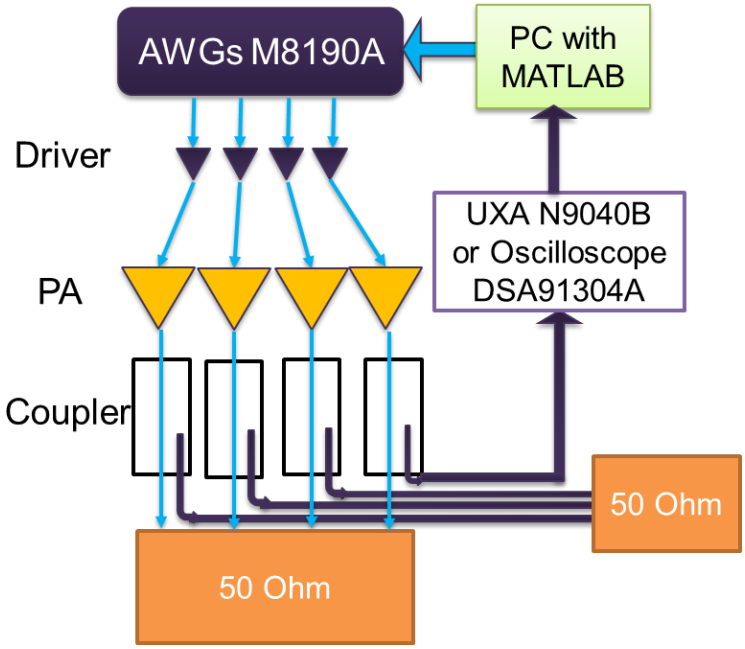

Fig. 5.1 PA array modulated signal measurement setup with 50 Ohm loaded

100MHz at	One channel On	Four channel On	20MHz at	One channel On	Four channel On
Before DPD NMSE (%)	9.3	9.3	Before DPD NMSE (%)	8.3	9.8
Before DPD ACPR (dB)	34.0 / 29.7	34.0 / 29.6	Before DPD ACPR (dB)	32.1 / 30.6	29.9 / 28.5
After DPD NMSE (%)	0.7	1.1	After DPD NMSE (%)	0.5	1.2
After DPD ACPR (dB)	50.5/ 49.8	50.2 / 49.9	After DPD ACPR (dB)	55.5 / 55.1	52.4 / 51.8

Table 5.1 PA array modulated signal measurement with 50 Ohm load

5.2 Antenna coupling effect investigation

Next, by employing the setup as shown in Fig. 5.2, where antenna array is used as load, the coupling effect of antenna array due to finite isolation can be studied. Since the performance of the four PAs are similar for clarifying the load modulation problem, in this thesis only one channel output is cap-

tured and linearized with SISO DPD when the other three channels are on or off. The measured isolation at PA output plane is -20 dB and the DPD coefficients are the same for all cases.

From table 5.2, the following observation and conclusion can be made: first, before SISO DPD, the difference in terms of ACPR and NMSE between in single-path scenario and MIMO scenario are very small: only less than 1 dB and 1% respectively. This means the distortion due to amplification is stronger than the distortion due to cross coupling, such that the cross coupling distortion is barely distinguishable [14]. Second, the performance degradation of SISO DPD in MIMO scenario shows that SISO DPD cannot compensate for the distortion created by cross coupling. And the degradation doesn't scale up with the signal bandwidth expansion when all other conditions are kept the same. This motivates people to employ more complex DPD architectures, such as multi-input DPD or dual input DPD [15]. However, the implementation of those DPD scheme is complicated and power consuming or even not feasible in real application. Therefore, SISO DPD still deserves exploration when applied in MIMO transmitter due to its simplicity and effectiveness. For instance, once some conditions are satisfied (these conditions will be shown in the following section), SISO DPD can still be used to linearize the whole chains successfully in MIMO transmitter with the lower cost compared to those complex DPD schemes. With such criteria, antenna and PA designers are able to design their parts specifically to achieve the optimal system performance.

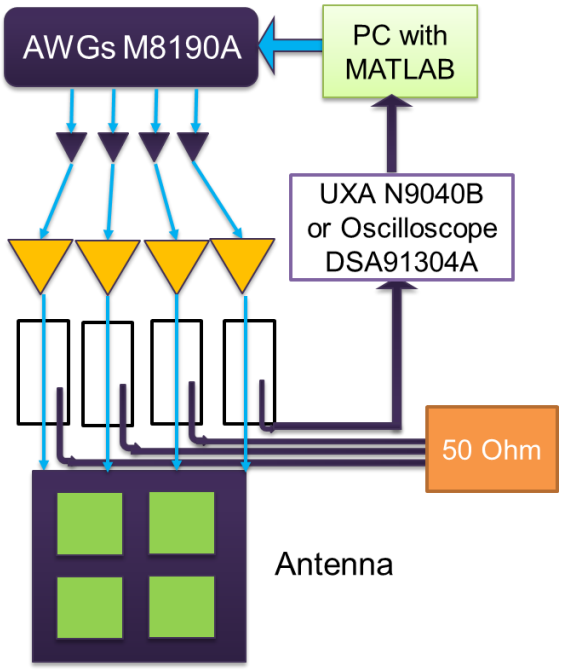

Fig. 5.2 PA array modulated signal measurement setup with antenna load

100MHz at 3.5GHz with	One channel On	Four channel On	20MHz at 3.5GHz with	One channel On	Four channel On
Before DPD NMSE (%)	9.3	10.3	Before DPD NMSE (%)	9.2	10.3
Before DPD ACPR (dB)	34.9/ 30.4	33.9 / 29.8	Before DPD ACPR (dB)	30.6 / 29.7	30.3 / 28.8
After DPD NMSE (%)	1.0	3.8	After DPD NMSE (%)	0.7	4.0
After DPD ACPR (dB)	48.3 /48.0	42.2 / 40.9	After DPD ACPR (dB)	53.0 / 52.1	41.1 / 40.7

Table 5.2 PA array modulated signal measurement with antenna load

5.3 Investigation for different isolation level and the extent of PA nonlinearity

From the section 4.4.4.2, we know that the distortion introduced by finite isolation between antenna elements cannot be handled by SISO DPD. Thus the various isolation level of antenna arrays can be used to investigate how the isolation levels can affect the SISO DPD linearization performance. Different values of attenuator are inserted between antenna array and PA array as shown in Fig.5.3, which is equivalent to improving the antenna isolation level. The corresponding simulation is also performed in ADS to justify this equivalence. In simulation, two well-designed antenna arrays with different isolation level, -19 dB in Fig.5.4 (a) and -28 dB in Fig.5.4 (b) and the -19 dB isolation array added with 9dB attenuators in Fig.5.4 (c) are used for illustration. The equivalent 9 dB isolation improvement can be realized by either adding 4.5 dB attenuators at each path of array, or by adding one 9 dB attenuator at the linearization target path. As a result, the coupled signal is attenuated by additional 9 dB. The four PAs have the same input magnitude but different phases. As shown in fig. 5.4, when the PAs are loaded with the 19 dB isolation antenna array, gain and AM-PM curves of the four paths show 0.8 dB and 5 degree variation between elements. However, when they are loaded with 28 dB isolation array, only 0.4 dB and 2 degrees variation in gain and AM-PM are observed, respectively. In addition, 19 dB array added with 9 dB attenuator also provides the similar dispersion reduction performance like 28 dB array. Considering the cost and design time, it is not feasible to fabricate the antennas with all levels of isolation. Fortunately the simulation shows that insertion of attenuators is an easy and effective way to offer the diversity.

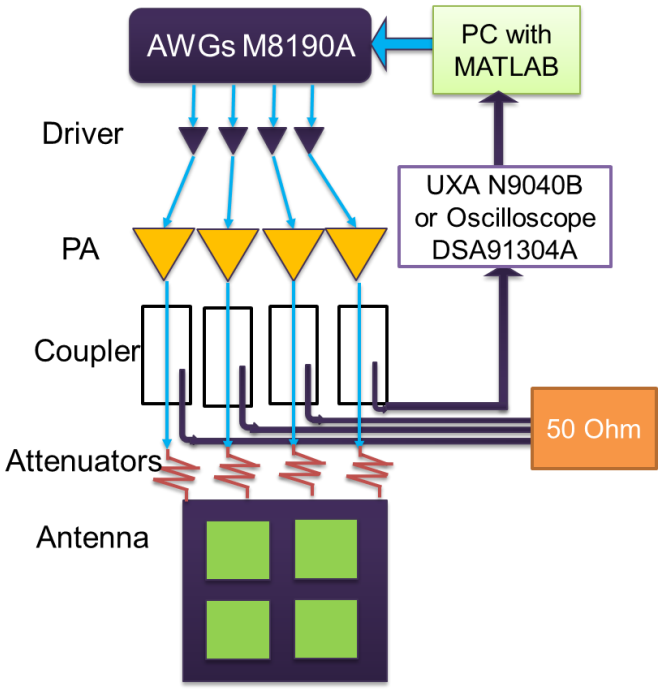

Fig. 5.3 PA array modulated signal measurement setup with antenna load and the insertion of attenuators

Consequently, with the addition of attenuators, we can provide the same PA array with different isolation level environment. On the other side, by backing off PA input level into linear region, we can enable PAs have different initial linearity level before DPD.

The measured ACPR after SISO DPD are summarized in table 5.3 and 5.4 for 100 and 20 MHz signals. When only one PA is on, the interferences from other paths don't exist, which corresponds to the infinite isolation level. When all four PAs are on without any attenuators, the antenna array itself offers the isolation baseline for reference. When attenuators are inserted between PAs and antennas in the linearization target path, the received signal leakage from other paths is reduced by the same amount as the attenuation, which is equivalent to improving isolation. Since -30 dB isolation is almost the lowest level a realistic antenna array can achieve, higher values of attenuator are not necessary. The measured -20 dB isolation from antenna array together with the addition of 9 dB isolation enhancement, are enough for real applications. All the four PAs are excited with four different and independent OFDM signals with the same average output power.

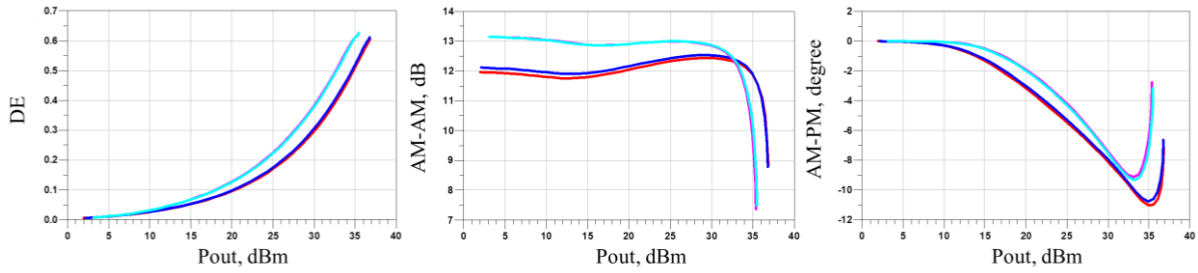

(a)

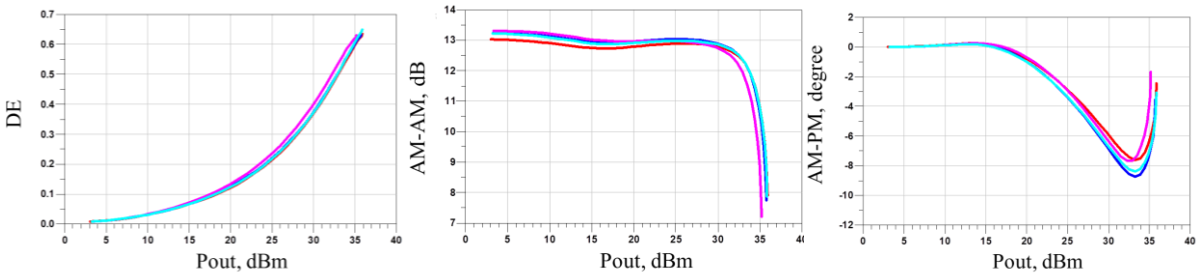

(b)

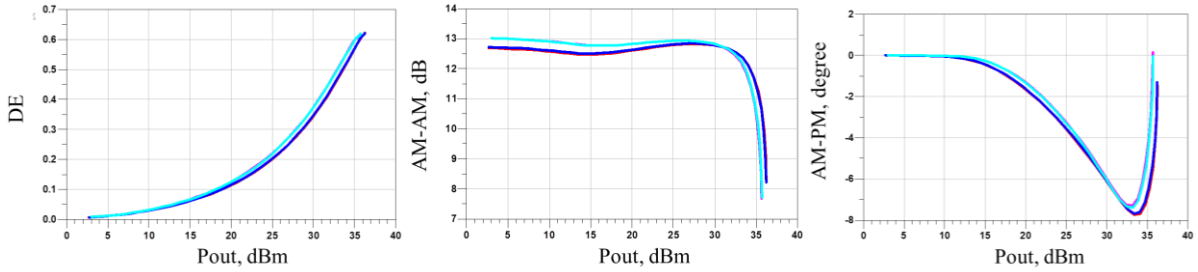

(c)

Fig. 5.4 PA array CW Simulation with the attenuator insertion in antenna array. (a) With -19 dB isolation antenna array. (b)With -28 dB isolation antenna array. (c) -19 dB isolation antenna array with 9 dB attenuation.

From each row in table 5.3 and 5.4, it is noticed that with the same level of PA linearity, when isolation is higher, SISO DPD in MIMO application performs more similar to that in signal-path case. Comparing each column, it can be seen that when the isolation is the same, more linear PAs have less residue after applying the same SISO DPD. Based on these two points above, it can be concluded that: to enable the SISO DPD linearize the PAs in a MIMO transmitter, both the linearity of the single PA and antenna coupling level need to be controlled. The red numbers in table 5.3 and 5.4 show that the higher the nonlinearity the PA has, the more stringent it becomes for the isolation requirement for the antenna array. This conclusion is true for both 20 MHz and 100 MHz cases.

Isolation level	Infinite	Base	+3 dB	+ 6 dB	+9 dB
32 dB ACPR before DPD	53.8	46.1	46.9	47.6	**51.8**
36 dB ACPR before DPD	55.0	50.4	**51.7**	53.1	54.3
40 dB ACPR before DPD	54.3	**51.6**	52.5	53.2	54.6

Table 5.3 ACPR in dB after SISO DPD with 20MHz OFDM signal for different isolation levels and initial PA nonlinearity

Isolation level	Infinite	Base	+3 dB	+ 6 dB	+9 dB
32 dB ACPR before DPD	49.5	44.9	47.5	48.9	**49.4**
36 dB ACPR before DPD	50.2	45.1	48.0	**49.6**	51.0
40 dB ACPR before DPD	50.6	47.4	**49.3**	50.3	51.5

Table 5.4 ACPR in dB after SISO DPD with 100MHz OFDM signal for different isolation levels and initial PA nonlinearity

Chapter 6
Conclusion and future work

6.1 Conclusion

The ever increasing demand for high system capacity motivates the employment of massive MIMO systems. The MIMO transmitter architecture proposes the stringent requirements for radio hardware. The removal of isolators imposes not only the mismatch between PA and antenna but also the load modulation brought by the leakage from other paths due to the finite isolation of the antenna array. Thus when the separately well-designed antenna and PA are connected directly, the analysis methodology should incorporate the nonlinearity generated from mismatch and cross coupling. The most relevant literatures studying the nonlinearity of MIMO transmitters are discussed in Chapter 2. They can be categorized into two families: the first emulates antenna coupling effects for PA nonlinearity by means of couplers, passive or active load-pull. The artificially added couplers can only provide a single fixed coupling in magnitude. The passive load-pull solely focuses on the static load mismatch. As for the active load-pull, this element-oriented system cannot offer any estimation of the array performance. The second group uses real antenna array based analysis. However, up to date, most work are either based on measurement of linear array and simulation of 2D array, or based on linear amplifiers excited by narrow band signals. Apparently, none of them represents the realistic PA-Antenna array in a massive MIMO transmitter. The main aim of this thesis is to propose and develop a realistic RF front end for MIMO transmitter to study the load modulation problem, where all the nonlinearity are included and manifested.

As the first step, different techniques to enlarge the patch antenna bandwidth and to reduce array isolation are discussed. Considering the ease of fabrication and scalability to a larger array, a wideband and high isolation 2×2 patch antenna array was designed for providing the appropriate load termination for PAs. The designed two-layer patch antenna array with added loop resonator achieved 400MHz bandwidth at 3.5 GHz, and -19 dB coupling level. As for the DUT, a Class-J PA array was designed and operated at high efficiency over 600MHz bandwidth at 3.5GHz. The excellent linearizability of the system can be seen by driven with 200MHz modulation bandwidth OFDM signal. The PA array has compact integration allowing to scale to larger array and direct connection with antenna.

Then with the designed antenna and PA array directly connected, this realistic RF front end is used to perform systematic measurement. PA board coupling effect is first studied and justified that this

minor effect doesn't mask the distortion of antenna coupling. Then the antenna coupling effect is researched in two dimensions: the isolation level of the antenna array and the PA nonlinearity extent before SISO DPD. It is found that the linearity of PA itself and antenna coupling level both need to be controlled to allow the SISO DPD to linearize the PAs in MIMO transmitter successfully. The higher the nonlinearity of the PA, the more stringent requirement it imposes on the isolation of the antenna array. This reminds the PA and antenna designers that the separately well-designed parts put together in a MIMO system environment do not necessarily have the expected performance. The system-oriented design is needed for optimal trade-off. Unfortunately, due to the limited time, only qualitative guidance was given for PA linearity and antenna isolation requirement.

6.2 Future work

Both antenna and PA show the frequency shift and discrepancy between simulation and measurement, which can be attributed to the three reasons: the inaccuracy of substrate properties used in simulation, the inaccuracy of large signal transistor model, the assembling error. The first effect can be released by pre-test on substrate properties with a product sample. The third effect can be minimized by professional assembling. Besides, taking into account for drivers' properties can also help to reduce the difference.

Based on the conclusions mentioned above, we know that the requirement on antenna isolation can be relaxed by more linear PA design. Quantitative analysis should be conducted from the system behavior modeling perspective such that more specific design guidance can be offered for PA and antenna designers.

Last but not least, reducing PA's load sensitivity helps to gain immunity of load modulation in MIMO scenario. Balanced PA topology offers the inherent load insensitivity due to the 90 degree phase shift between the outputs of the two amplifiers inside the total PA [36], and it would be worthwhile to investigate the performance improvement under the load variation environment in MIMO transmitters.

Reference

[1] Y. Ji, J. Zhang, Y. Xiao and Z. Liu, "5G flexible optical transport networks with large-capacity, low-latency and high-efficiency," in China Communications, vol. 16, no. 5, pp. 19-32, May 2019.

[2] G. Liu, Y. Huang, F. Wang, J. Liu and Q. Wang, "5G features from operation perspective and fundamental performance validation by field trial," in China Communications, vol. 15, no. 11, pp. 33-50, Nov. 2018.

[3] A. F. Molisch and M. Z. Win, "MIMO systems with antenna selection," in IEEE Microwave Magazine, vol. 5, no. 1, pp. 46-56, March 2004.

[4] S. Shinjo, K. Nakatani, K. Tsutsumi and H. Nakamizo, "Integrating the Front End: A Highly Integrated RF Front End for High-SHF Wide-Band Massive MIMO in 5G," in IEEE Microwave Magazine, vol. 18, no. 5, pp. 31-40, July-Aug. 2017.

[5] C. Fager, T. Eriksson, F. Barradas, K. Hausmair, T. Cunha and J. C. Pedro, "Linearity and Efficiency in 5G Transmitters: New Techniques for Analyzing Efficiency, Linearity, and Linearization in a 5G Active Antenna Transmitter Context," in IEEE Microwave Magazine, vol. 20, no. 5, pp. 35-49, May 2019.

[6] Y. Palaskas et al., "A 5-GHz 108-Mb/s 2x2 MIMO Transceiver RFIC With Fully Integrated 20.5-dBm P_{1dB} Power Amplifiers in 90-nm CMOS," in IEEE Journal of Solid-State Circuits, vol. 41, no. 12, pp. 2746-2756, Dec. 2006.

[7] S. A. Bassam, M. Helaoui and F. M. Ghannouchi, "Crossover Digital Predistorter for the Compensation of Crosstalk and Nonlinearity in MIMO Transmitters," in IEEE Transactions on Microwave Theory and Techniques, vol. 57, no. 5, pp. 1119-1128, May 2009.

[8] S. Amin, P. N. Landin, P. Händel and D. Rönnow, "Behavioral Modeling and Linearization of Crosstalk and Memory Effects in RF MIMO Transmitters," in IEEE Transactions on Microwave Theory and Techniques, vol. 62, no. 4, pp. 810-823, April 2014.

[9] P. Jaraut, M. Rawat and F. M. Ghannouchi, "Composite Neural Network Digital Predistortion Model for Joint Mitigation of Crosstalk,I/Q Imbalance, Nonlinearity in MIMO Transmitters," in IEEE Transactions on Microwave Theory and Techniques, vol. 66, no. 11, pp. 5011-5020, Nov. 2018.

[10] D. Nopchinda and K. Buisman, "Emulation of array coupling influence on RF power amplifiers in a measurement setup," 2016 87th ARFTG Microwave Measurement Conference (ARFTG), San Francisco, CA, 2016, pp. 1-4.

[11] S. K. Dhar, A. Abdelhafiz, M. Aziz, M. Helaoui and F. M. Ghannouchi, "A Reflection-Aware Unified Modeling and Linearization Approach for Power Amplifier Under Mismatch and Mutual Coupling," in IEEE Transactions on Microwave Theory and Techniques, vol. 66, no. 9, pp. 4147-4157, Sept. 2018.

[12] C. Fager, X. Bland, K. Hausmair, J. Cahuana, and T. Eriksson, “Prediction of smart antenna transmitter characteris-tics using a new behavioral modeling approach,” in MTT-S International Microwave Symposium Digest, Tampa, FL, Jun. 2014, pp. 1–4.

[13] F. M. Barradas, P. M. Tomé, J. M. Gomes, T. R. Cunha, P. M. Cabral and J. C. Pedro, "Power, Linearity, and Efficiency Prediction for MIMO Arrays With Antenna Coupling," in IEEE Transactions on Microwave Theory and Techniques, vol. 65, no. 12, pp. 5284-5297, Dec. 2017.

[14] K. Hausmair et al., "Prediction of Nonlinear Distortion in Wideband Active Antenna Arrays," in IEEE Transactions on Microwave Theory and Techniques, vol. 65, no. 11, pp. 4550-4563, Nov. 2017.

[15] K. Hausmair, P. N. Landin, U. Gustavsson, C. Fager and T. Eriksson, "Digital Predistortion for Multi-Antenna Transmitters Affected by Antenna Crosstalk," in IEEE Transactions on Microwave Theory and Techniques, vol. 66, no. 3, pp. 1524-1535, March 2018.

[16] C. Fager, K. Hausmair, K. Buisman, K. Andersson, E. Sienkiewicz and D. Gustafsson, "Analysis of nonlinear distor-tion in phased array transmitters," 2017 Integrated Nonlinear Microwave and Millimetre-wave Circuits Work-shop (INMMiC), Graz, 2017, pp. 1-4.

[17] N. Tervo, M. E. Leinonen, J. Aikio, T. Rahkonen and A. Pärssinen, "Analyzing the Effects of PA Variations on the Performance of Phased Array Digital Predistortion," 2018 IEEE 29th Annual International Symposium on Personal, Indoor and Mobile Radio Communications (PIMRC), Bologna, 2018, pp. 215-219.

[18] A. Vaezi, A. Abdipour, A. Mohammadi and F. M. Ghannouchi, "On the Modeling and Compensation of Backward Crosstalk in MIMO Transmitters," in IEEE Microwave and Wireless Components Letters, vol. 27, no. 9, pp. 842-844, Sept. 2017.

[19] A. G. Derneryd, I. Karlsson, "Broadband Microstrip Antenna Element and Array", IEEE Trans. Antennas Propagat., vol. AP-29, no. 1, pp. 140-141, January 1981.

[20] S. Egashira and E. Nishiyama, "Stacked microstrip antenna with wide bandwidth and high gain," in IEEE Transactions on Antennas and Propagation, vol. 44, no. 11, pp. 1533-1534, Nov. 1996.

[21] S. Wi, Y. Lee and J. Yook, "Wideband Microstrip Patch Antenna With U-Shaped Parasitic Elements," in IEEE Transactions on Antennas and Propagation, vol. 55, no. 4, pp. 1196-1199, April 2007.

[22] H. Wang, X. B. Huang and D. G. Fang, "A Single Layer Wideband U-Slot Microstrip Patch Antenna Array," in IEEE Antennas and Wireless Propagation Letters, vol. 7, pp. 9-12, 2008.

[23] H. Wong, K. K. So and X. Gao, "Bandwidth Enhancement of a Monopolar Patch Antenna With V-Shaped Slot for Car-to-Car and WLAN Communications," in IEEE Transactions on Vehicular Technology, vol. 65, no. 3, pp. 1130-1136, March 2016.

[24] K. M. Luk, C. L. Mak, Y. L. Chow and K. F. Lee, "Broadband microstrip patch antenna," in Electronics Letters, vol. 34, no. 15, pp. 1442-1443, 23 July 1998.

[25] Y. Shi, J. Liu and Y. Long, "Wideband Triple- and Quad-Resonance Substrate Integrated Waveguide Cavity-Backed Slot Antennas With Shorting Vias," in IEEE Transactions on Antennas and Propagation, vol. 65, no. 11, pp. 5768-5775, Nov. 2017.

[26] Shaoqiu Xiao, Bing-Zhong Wang, Wei Shao and Yan Zhang, "Bandwidth-enhancing ultralow-profile compact patch antenna," in IEEE Transactions on Antennas and Propagation, vol. 53, no. 11, pp. 3443-3447, Nov. 2005.

[27] E. Nishiyama, M. Aikawa, and S. Egashira, “Stacked microstrip antenna for wideband and high gain,” IEE Proc.- Microw. Antennas Propag., vol. 151, no. 2, pp. 143–148, Apr. 2004.

[28] Xia R, Qu S, Jiang Q, Li P, Nie Z. An efficient decoupling feeding network for two-element microstrip antenna array. IEEE Transactions on Antennas and Wireless Propagation letters. 2015; 14:871–4.

[29] Zhang S, Pedersen G. Mutual coupling reduction for UWB MIMO antennas with a wideband neutralization line. IEEE Antennas and Wireless Propagation Letter. 2015; 15:166–9.

[30] Islam MT, Alam MS. Compact EBG structure for alleviating mutual coupling between patch antenna array elements. Progress in Electromagnetics Research. 2013; 137:425–38.

[31] A. Suntives and R. Abhari, ``Miniaturization and isolation improvement of a multiple-patch antenna system using electromagnetic bandgap structures," Microw. Opt. Technol. Lett., vol. 55, no. 7, pp. 1609_1612, 2013.

[32] Suwailam MMB, Boybay MS, Ramahi OM. Single-Negative (SNG) metamaterials for mutual coupling reduction in high profile antennas. Antennas and Propagation Society International Symposium (APSURSI); 2009. p. 1-4.

[33] M. G. N. Alsath, M. Kanagasabai, and B. Balasubramanian, “Implementation of slotted meander-line resonators for isolation enhancement in microstrip patch antenna arrays,” IEEE Antennas Wireless Propag. Lett. vol. 12, no., pp. 15–18, 2013.

[34] B. L. Dhevi, K. S. Vishvaksenan and K. Rajakani, "Isolation Enhancement in Dual-Band Microstrip Antenna Array Using Asymmetric Loop Resonator," in IEEE Antennas and Wireless Propagation Letters, vol. 17, no. 2, pp. 238-241, Feb. 2018.

[35] S. C. Cripps, P. J. Tasker, A. L. Clarke, J. Lees and J. Benedikt, "On the Continuity of High Efficiency Modes in Linear RF Power Amplifiers," in IEEE Microwave and Wireless Components Letters, vol. 19, no. 10, pp. 665-667, Oct. 2009.

[36] S. Sinha, C. V. N. Rao and D. Pujara, "Balanced Power Amplifier Protection Against Load Mismatch," in IEEE Microwave and Wireless Components Letters, vol. 28, no. 2, pp. 165-167, Feb. 2018.